

Møller Polarimetry for CEBAF Hall C

INAUGURAL-DISSERTATION

zur

Erlangung der Würde eines Doktors der Philosophie,
vorgelegt der Philosophisch-Naturwissenschaftlichen Fakultät
der Universität Basel

von

MATTHIAS LOPPACHER

aus Basel

Basel 1996

Genehmigt von der Philosophisch-Naturwissenschaftlichen Fakultät

auf Antrag der

Herren Professor Dr. I. Sick und PD Dr. H. Mühry.

Basel, den 30. April 1996

Prof. Dr. Hans-Christoph Im Hof

Dekan

Acknowledgments

I want to express my gratitude to Prof. Dr. Ingo Sick for giving me the opportunity to work with his group during the past five years, for his advice and continuing interest in my scientific work.

I am also thankful to Laurens de Bever, Stephan Robinson and Jie Zhao for their collaboration and interest in the development of the Møller Polarimeter. Especially in Virginia we have been a great team! In addition to the physics we enjoyed performances of the Virginia Symphony, many walks and bike trips. I will always remember the good old times we spent together in the United States.

I owe a big thanks to Joe Mitchell for the constantly improving collaboration. Apart from physics he also provided great cultural tips. With a wonderful bike trip we experienced the blue ridge mountains where I returned many times with my Swiss friends.

Thank you to Al Tobias for his help in organizing this, that and more! He made working at University of Virginia easy for us. His kind offers to continue many jobs we could not finish were a great help to us!

A special thank is expressed to my office mates, Heinz Anklin, Günther Kubon and Philipp Steiner for many challenging discussions and all the tea they served. We have been keeping a friendly atmosphere during all the times and also enjoyed many mutual invitations.

A very special thank to my girl friend Barbara! Her love and encouragement as well as her always positive psychological and mental advices have been the best privat support I could get. She – during the hard times – relieved me from any house keeping duties.

Last but not least thank you to my parents, Elisabeth and Walter Loppacher-Sutter, for the encouragement and personal support, without which I would never have gotten so far.

Contents

1	Introduction	1
1.1	Generalities	1
1.2	Theoretical considerations	2
1.3	Some previous measurements	3
2	Lay-out of the CEBAF polarimeter	5
2.1	Polarimeter optics	5
2.2	Detectors	9
2.3	Electronics	12
3	The Møller target	14
3.1	Different ways of magnetizing	14
3.2	Precise saturation values for our application	16
3.2.1	Ferromagnetism: temperature dependence and domain structure . .	17
3.2.2	Out of plane magnetization	18
3.2.3	Correction terms for strong B-fields	19
4	Measuring magnetization with the Kerr effect	20
4.1	The Polar Kerr effect	20
4.2	Setup of the Kerr apparatus	22
4.3	Saturation measurements	24
4.4	Depolarization measurements	25
4.5	Power deposition in the target	28
5	Monte Carlo Simulations	30

5.1	Mott background	30
5.2	Multiple scattering	31
5.3	Levchuk effect	33
6	Outlook	37
A	Errors in the determination of beam polarization P_b	38
A.1	Systematic error in $\overline{A_{zz}}$	39
A.1.1	Accuracy of the Levchuk correction	39
A.1.2	Geometrical alignment and beam optics	39
A.2	Error in target polarization P_t	41
A.3	Statistical errors and count rate estimates	42
B	Tuning procedure for the Møller Polarimeter	44
B.1	Timing	44
B.2	Magnet and beam optics	45
B.3	Quadrupole settings	49
C	CADs	50
D	Suppliers	66
	Bibliography	68

List of Figures

2.1	Møller setup using only one quadrupole.	6
2.2	Distribution of Møller electrons for a setup with one quadrupole.	7
2.3	Møller setup using two quadrupoles.	7
2.4	Distribution of Møller electrons for a setup with two quadrupoles.	8
2.5	Quadrupole currents for 1 – 6 GeV beam energy.	8
2.6	Arrangement of the detectors.	9
2.7	Actual sizes and acceptances of the detectors	10
2.8	Simulations for hodoscope and lead glass detectors.	11
2.9	Logic setup of the electronics.	12
2.10	Hodoscope pattern for correct tuning.	13
3.1	In-plane target; magnetization measurement with pick-up coils.	15
3.2	Out-of-plane target: a priori saturated.	15
3.3	Magnetical saturation; experimental data and the $T^{\frac{3}{2}}$ law.	17
3.4	Different angles between the foil plane and the B-field.	18
3.5	Saturation for small foil alignment error.	19
3.6	Saturation corrections due to a large B-field.	19
4.1	Polar Kerr effect: Rotation angle as a function of wave length.	21
4.2	Setup of the kerr apparatus.	22
4.3	Schematic view of Kerr effect on modulated polarization.	23
4.4	Effect of magnetization on signal entering the Lock-in amplifier.	23
4.5	Kerr measurement: a complete ramp up-down to 3 Tesla.	24
4.6	Saturation point at 2.2 Tesla.	25

4.7	Setup for a depolarization test.	25
4.8	Depolarization tests using a heat tip.	26
4.9	Polarization dependent on foil temperature.	27
4.10	Beam spot temperature depending on beam radius.	28
4.11	Magnetization deviation for different beam spots.	28
4.12	Relative polarization as a function of beam current.	29
5.1	Mott background	30
5.2	Multiple scattering at the detectors.	32
5.3	Multiple scattering of the beam.	32
5.4	Event distribution for coincidence of lead glass detectors.	33
5.5	Event distribution for 'coincidence' of hodoscope	34
5.6	A_{zz} distribution for coincident detectors (deflection direction).	35
5.7	A_{zz} distribution (orthogonal to deflection direction).	35
A.1	Error in $\overline{A_{zz}}$ as a function of the detector misalignment.	40
A.2	Error in $\overline{A_{zz}}$ as a function of beam misalignment.	41
B.1	Hodoscope event pattern for perfect tuned quadrupoles.	45
B.2	Hodoscope event pattern for a too small value of the large quadrupole.	45
B.3	Hodoscope event pattern for a too small value of the small quadrupole.	46
B.4	Response of splitted hodoscope channels for beam up/down	46
B.5	Hodoscope event pattern with beam 5 mm off center (to the left).	47
B.6	Møller event distribution: correct tuned beam.	47
B.7	Møller event distribution: beam + 5 mm to the left.	48
B.8	Møller event distribution: beam + 1 mm up	48
C.1	Target: side view	50
C.2	Target rail system	51
C.3	Target chamber: side view	52
C.4	Target chamber: top view	53
C.5	Collimator vacuum can	54

C.6	Small vacuum can	55
C.7	Y-vacuum can	56
C.8	Arrangement on the detector platform	57
C.9	Table top for detectors	58
C.10	Hodoscope mounting frame	59
C.11	Hodoscope PM plane 1	60
C.12	Hodoscope PM plane 2	61
C.13	Hodoscope side plane 1	62
C.14	Hodoscope side plane 2	63
C.15	Hodoscope PM clamps	64
C.16	System to glue hodoscope together	65

List of Tables

1.1	Previous polarization measurements.	4
2.1	Møller scattering angles in the lab frame	6
2.2	NIM units	13
2.3	CAMAC-ECL units	13
3.1	Magnetization/polarization values for the out-of-plane target	16
5.1	Møller lab angle and multiple scattering for different beam energies.	31
5.2	Beam loss, due to multiple scattering	32
5.3	$\overline{A_{zz}}$ for different beam energies.	36
5.4	$\overline{A_{zz}}$ dependence on MS.	36
A.1	Effective $\overline{A_{zz}}$ for different beam energies.	39
A.2	Errors due to misalignment or mistuning.	40
A.3	Error of the target polarization	41
A.4	Count rate and measuring time for $\frac{\Delta P}{P}=1\%$ and 4 GeV beam energy.	43
A.5	Cross section and measuring time for different beam energies.	43
B.1	Calculated quadrupole current settings	49

Chapter 1

Introduction

1.1 Generalities

In probing fundamental properties of nuclei and the nucleon and corresponding theoretical models, electron beam accelerators are an essential tool. The latest class of experiments to test QCD based models require a spin polarized beam and/or target because spin observables are sensitive to details normally not accessible when using an unpolarized beam. New polarized electron sources based on photoemission from strained GaAs are capable of producing significant current of electrons polarized up to 85 % and open up the possibility to measure the spin observables which will significantly improve our understanding of nucleons and nuclei.

Taking the full advantage of a high quality polarized electron beam requires to measure its polarization with the same quality. A common technique, electron-nucleus or Mott scattering, is used at energies below 1 MeV, where the cross-section is relatively large. This technique is most often used to measure the polarization before passing the electrons to the main accelerator. It suffers from relatively large systematic errors [F186] and polarization changes caused by the transport in the main accelerator remain undetected. Performing an accurate polarization measurement needs to be done at the final electron energy directly before the experiment.

Measuring the spin polarization of a high energy electron beam can be done using the following techniques:

- Electron – photon scattering (Compton back-scattering)
- production of synchrotron radiation (by deflection of the beam)
- Electron – electron scattering (Møller scattering)

The first technique, Compton back-scattering is 'non-destructive' and therefore can be performed in parallel with physics experiments. The draw back is a very small rate of detected photons. For high beam intensity machines (such as SLC) or storage rings (such as HERA) the Compton back-scattering technique has been used successfully. A priori a very accurate measurement is possible.

The second technique, production of synchrotron radiation, suffers from the same disadvantage; due to the very small cross-section a high beam current is required which most polarization experiments exclude. Up to now no experimental experience has been gained but from the theoretical point of view a precision measurement is possible.

The third, most established, way is by electron – electron or Møller scattering which has been used under many situations and over a wide range of energies, see Table 1.1. Beam electrons scatter off the polarized electrons of a thin magnetized ferromagnetic foil. The foil polarization is conventionally determined with a flux measurement which is limited to an accuracy of about 2% [Fe96]. This third type of polarimetry is discussed in this thesis and a novel system to reduce the error in the knowledge of the target foil polarization is introduced.

1.2 Theoretical considerations

As Møller polarimetry is based on $\vec{e} + \vec{e} \rightarrow e + e$ scattering, a pure QED process, the cross-section can be calculated to very high precision. For the relevant longitudinal spin orientations ¹ the center of mass (CM) cross-section is expressed as:

$$\frac{d\sigma}{d\Omega} = \frac{d\sigma_o}{d\Omega} \left[1 + P_Z^T P_Z^B A_{ZZ}(\theta) \right] \quad (1.1)$$

where $\frac{d\sigma_o}{d\Omega}$ is the unpolarized cross-section, $A_{ZZ}(\theta)$ the analyzing power, P_Z^T and P_Z^B the longitudinal target and beam polarization respectively. One can effectively measure the beam polarization by comparing the cross-section asymmetry for beam and target spins aligned parallel and anti-parallel:

$$A = \frac{\frac{d\sigma^{\uparrow\uparrow}}{d\Omega} - \frac{d\sigma^{\uparrow\downarrow}}{d\Omega}}{\frac{d\sigma^{\uparrow\uparrow}}{d\Omega} + \frac{d\sigma^{\uparrow\downarrow}}{d\Omega}} = A_{ZZ}(\theta) P_Z^B P_Z^T. \quad (1.2)$$

At 90 degrees (CM), the analyzing power is large, $A_{ZZ} = -\frac{7}{9}$, and so is the cross-section, $\left. \frac{d\sigma_o}{d\Omega} \right|_{lab} = 179$ mbarn. Further, these quantities are energy independent for large γ ($\frac{E}{m_e c^2}$) [Fe96].

The main background sources are: the radiative tail of electron-nucleus scattering from the nuclei in the Møller target foil, and low energy electrons and photons produced in bremsstrahlung related processes in the foil and vacuum windows.

Only recently was it realized [Le94] that the atomic motion of the bound target electrons is significantly affecting the analyzing power of a Møller polarimeter. In fact the momentum distribution (\vec{p}_i) of the target electrons modifies, and thereby introduces an uncertainty to, the lab scattering angle [Sw95]: $\theta' = \theta_o \sqrt{1 + \frac{\vec{p}_i \cdot \hat{z}}{m_e}}$, an effect whose scale is determined

¹In experiments using polarized high energy electrons, only the longitudinal electron polarization is of interest. Transverse polarizations are suppressed by the Lorentz factor $\frac{1}{\gamma}$ [Do86]. Therefore experiments with polarized electron beams will be done with longitudinal polarization.

by the electron mass! The inner shell (unpolarized) electrons have much larger momenta than those in the outer shells (the electrons carrying the polarization). As a result, a detector which resolves the θ angle of the scattered electrons has a different acceptance for scattering off a polarized versus unpolarized target electron.

1.3 Some previous measurements

There have been many Møller polarimeters over the years, see Table 1.1. Starting with single arm measurements the development turned to the coincidence mode which significantly reduced the background. New detectors which provided accurate timing and energy information again improved the situation. Common to all of these polarimeters was the technique used to measure the target polarization, which nowadays contributes the largest error. Below I discuss some measurements which illustrate the development.

P.S. Cooper performed the first polarization measurement using Møller polarimetry at high energies (several GeV) [Coo75]. This was a single arm measurement using a high resolution spectrometer. This measurement, with an error of 4%, was for more than a decade the most accurate one. The motivation of this work was to demonstrate the technique of Møller polarimetry and to investigate the spin-dependence of a purely quantum electrodynamic (QED) process. The experiment served as a check of spin-dependence in QED which before had not been studied at energies above the muon decay [Sc67].

B. Wagner performed systematic studies using Møller polarimetry [Wa86]. In order to reduce the background he detected the two electrons in coincidence. As detectors gas Cerenkov counters were used which allow only discrimination against slow particles. Wagner's Møller polarimeter was the first one operating in coincidence mode at a small duty cycle.

In 1995 the Basel group performed high precision polarization measurements at SLAC [Fe95]. To reduce the contribution of low energy background events, lead glass total absorption counters were used in coincidence mode. The low duty cycle of the SLAC machine resulted in a very high instantaneous rate, which required segmented detectors and fast electronics. A final uncertainty in the order of 2% was achieved. The main contribution came from the uncertainty of the Møller foil polarization.

Comparing beam polarization measurements performed in the past shows, that not a lot of progress has been made until recently. A list of polarization measurements performed in the past is given below.

Year	Facility	Max. E_{beam} (GeV)	Limitation	detectors		Uncert. $\Delta P/P$	Ref.
				Single	Coinc.		
1975	SLAC	19.4	foil/stat/bck	✓		4%	[Co75]
1976	SLAC-E80	12.9	foil/stat/bck	✓		12%	[Al76]
1978	SLAC-E122	22.2	foil/stat/bck	✓		5.5%	[Pr78]
1982	SLAC-E130	22.7	foil/stat		✓	4%	[Ba83]
1984	Bonn	2.0	stat		✓	12%	[Br85]
1986	Mainz	0.071 → 0.35	foil/stat		✓	4%	[Wa90]
1990	MAMI	0.185 → 0.84	foil/bck		✓	4%	[Wa90]
1992	Bates	0.574	stat/bck	✓		12%	[Ar92]
1992	SLAC-linac	46.6	foil/bck	✓		4.2%	[Sw95]
1993	SLAC-E142	26	foil/bck	✓		4%	[An93]
1995	Bates	0.868	stat/bck		✓	5%	[Be95]
1995	SLAC-E143	29	foil		✓	2%	[Fe97]

Table 1.1: Previous polarization measurements. Limitations: foil = Møller target polarization, stat = statistics, bck = background.

In the latest measurement the error of the Møller target polarization dominated. In this thesis we especially address this problem. A new method of magnetizing a ferromagnetic foil and surveying its magnetization is discussed. This reduces the error of the foil polarization to below 1% and a final accuracy of the beam polarization measurement of better than $\pm 1\%$ can be reached. Besides that, a special magneto-optic setup allows for measurements of the polarization over a very wide energy range (1 – 6 GeV) at currents starting from a few 10 nA up to 50 μ A. Up to now, no polarimeter has been able to cover such a large energy and current range.

Chapter 2

Lay-out of the CEBAF polarimeter

The requirements for the planned experiments employing polarized beam differ in many ways and so do the ones for the beam line polarimeter. To become the standard tool for polarization measurements at CEBAF hall C the following aims and capabilities were required:

- **Measurement of the beam polarization with a relative error of less than 1%**
- Beam currents from 10 nA up to 50 μ A, without loss of accuracy due to heating up of the foil.
- Beam energies from 1 GeV to 6 GeV.
- Acceptable measuring times for low currents.
- One setup with fixed target and detector positions for the whole energy range.
- Provisions for easy adjustments and cross checks.

To reach the goal of 1% relative error we built a coincidence polarimeter. Furthermore we developed a new Møller target, an iron foil polarized out of plane. Finally the polarization of the Møller target will be surveyed online with a laser system.

2.1 Polarimeter optics

The standard setup of Møller polarimeters involves a single quadrupole between the Møller target and the detectors, similar to the setup shown in Figure 2.1. The quadrupole is used to get some additional separation between the main electron beam and the Møller electrons. Scattering angles for different beam energies are given in Table 2.1.

As pointed out in the list of desired capabilities given above, a fixed target and detector position was required as neither the target (superconducting magnet plus laser system)

E_{Beam} (GeV)	scattering angle (lab)	E_{Beam} (GeV)	scattering angle (lab)
1	1.83°	2	1.29°
3	1.06°	4	0.92°
5	0.82°	6	0.75°

Table 2.1: Møller scattering angles in the lab frame

nor the detectors (2 tons of shielding material) are easily movable. Additionally we need vacuum up to the detectors which would make movable parts cumbersome and costly. With this boundary condition and the desired energy range, simulations for just one large quadrupole (the available Argonne quad) were made. The result was unsatisfactory as explained below.

To get the largest separation the quadrupole was set as far away from the target as the 1 GeV rays allow, without hitting the quadrupole. The setup is shown in Figure 2.1.

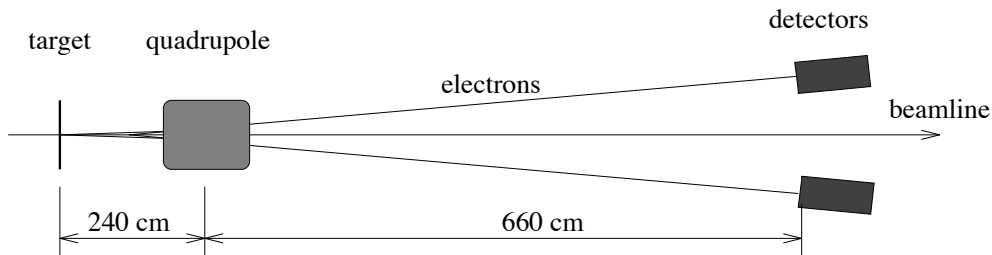


Figure 2.1: Setup for just one quadrupole, using the Argonne 10Q36 magnet

This setup does not produce much spread at higher energies. The distribution of the 90° CM scattered Møller electrons, which should form an ellipse on the x,y-detector plane, collapses to a line for energies around 2 GeV as shown in Figure 2.2. In such a situation, no positional information (derived from a hodoscope) can be extracted. Furthermore, the distribution of electrons chosen by the acceptance of one detector becomes very large at the place of the second detector. This requires one detector to be far bigger than the other one, which worsens the signal to noise ratio.

Obviously, a setup with only one quadrupole can not produce the desired results. Therefore a setup with two quadrupoles was simulated. Basically two quadrupoles are the magnetic counterpart of a real optics lens. They can focus or defocus all electrons whereas a single quadrupole focuses in one plane and defocuses in the other. Advantages of a two quadrupole setup are:

- We can produce the desired elliptical shape (relation between the two half-axes) as long as the strength of our magnets is sufficient. This allows an optimal hodoscope resolution and an optimal signal to noise ratio over the entire energy range.

- We can shift the second quadrupole further away from the target (maximal deflection is reached when placed midway between target and detectors). The 1 GeV rays (producing the largest angle) can be focussed by the first quadrupole through the second one.
- We can accommodate accelerator upgrades: for energies higher than 6 GeV, one can still use the polarimeter up to about 7.5 GeV by compromising with the hodoscope resolution.

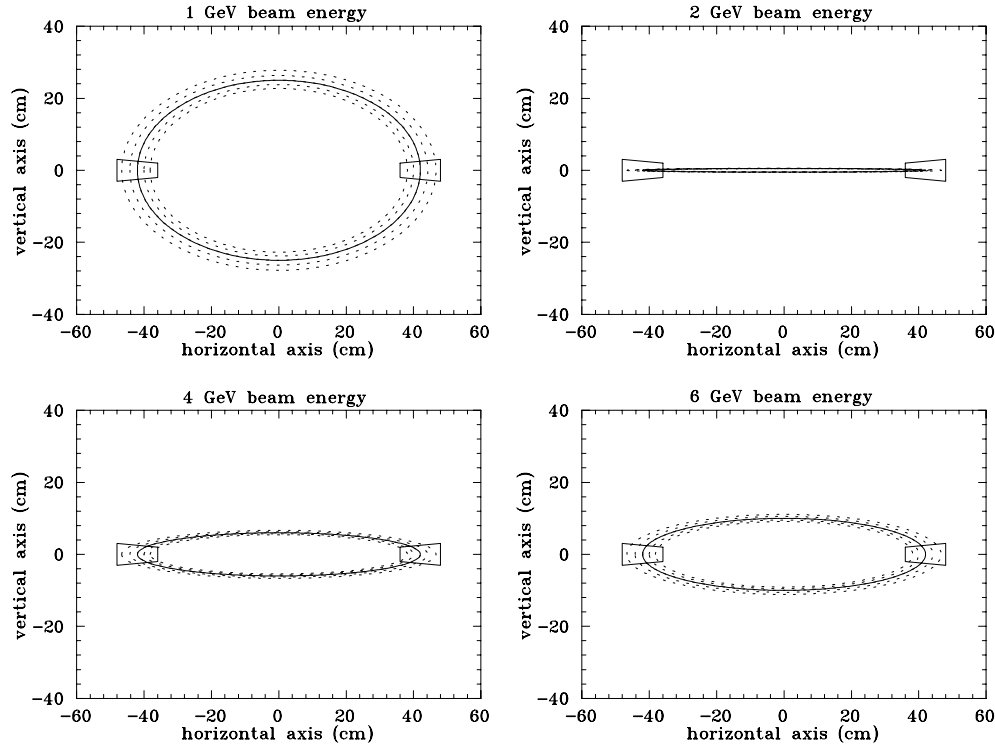


Figure 2.2: Distribution of Møller electrons around 90 degrees CM scattering angle in the plane of the detectors for the one-quadrupole setup. For energies around 2 GeV a collapse of the ellipse to a line occurs. The detectors are indicated by the polygons which are placed 42 cm apart from the beam line

The final polarimeter design involves two quadrupoles where the small one is situated 1m after the target and the large one 3.2m after the target, as seen in Figure 2.3.

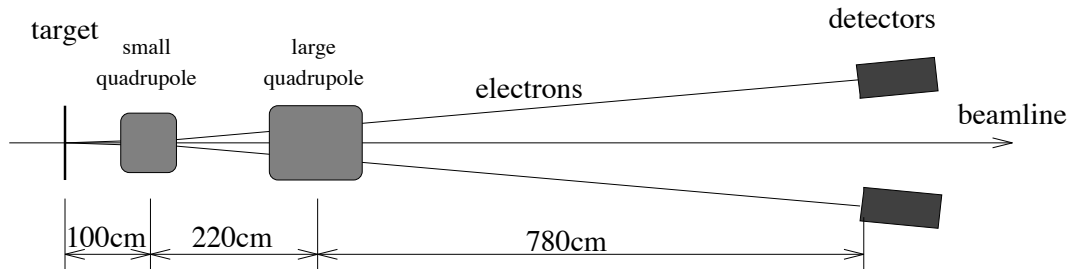


Figure 2.3: Two-quadrupole setup employing a small quadrupole (10cm inner diameter, 25cm effective length, 0.4 Tesla tip field) and the larger 10Q36 Argonne quadrupole

The simulation program Raytrace [Ray80] was used to show, that a satisfactory separation between the 90° CM Møller electrons and the beam line is possible. An ellipse with a horizontal axis of 49 cm and a vertical axis of 17 cm can be achieved for all energies between 1 and 6 GeV. The resulting Møller electron distribution is shown in Figure 2.4 for two beam energies.

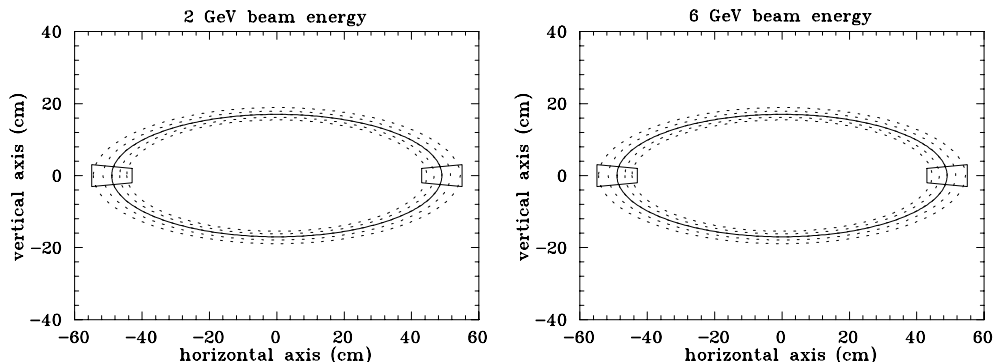


Figure 2.4: Distribution of Møller electrons around 90 degrees CM scattering angle in the plane of the detectors. The two-quadrupole setup allows us to produce a desired distribution of Møller electrons for all energies. A horizontal spread of 49 cm and a vertical spread of 17 cm has been chosen. The detectors are indicated by the small trapezoids and are placed 49 cm apart from the beam line

The chosen detector areas are shown in Figure 2.8. The optimized settings for the quadrupole currents are shown in Figure 2.5.

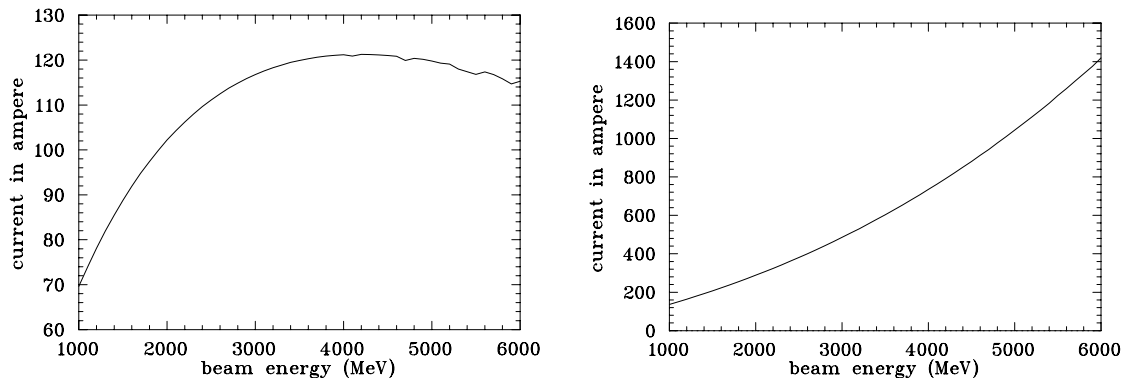


Figure 2.5: Quadrupole current settings: For both quadrupoles a B versus I calibration was used to correct for nonlinearities (see also Table B.1).

2.2 Detectors

The goal for our detector system is to achieve the best signal to noise ratio possible, which is done by suppressing background as much as possible. In order to suppress the Mott background we use two detectors in coincidence, Figure 2.3. A very narrow coincidence time gate of 5 ns reduces the accidental background. Shower counters, which also provide energy information, allow us to suppress any low energy background. A hodoscope delivers position information which will be used for checks and adjustments only. The basic arrangement of detectors and collimator is shown in Figure 2.6.

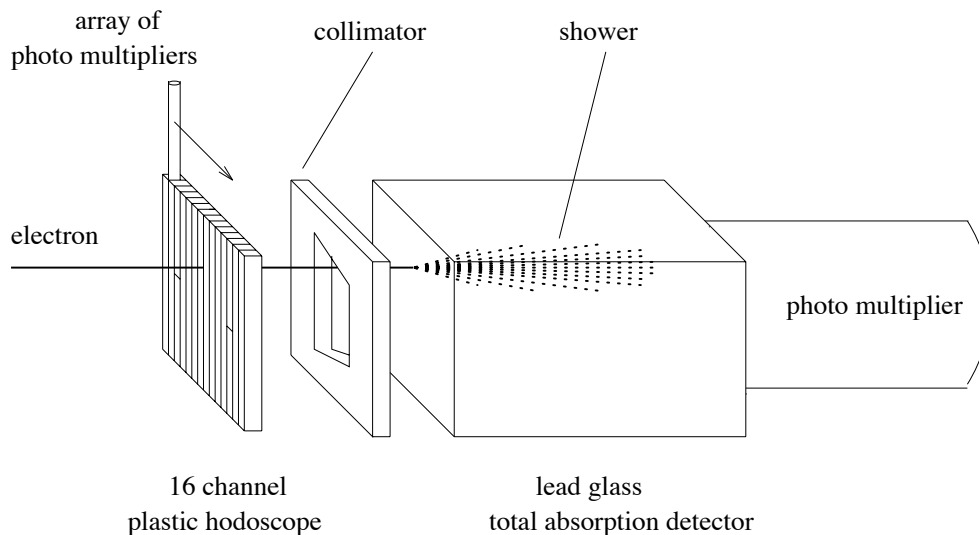


Figure 2.6: Detectors: A lead glass total absorption detector gives timing and energy information which is used for the main coincidence. The 16 channel plastic scintillator hodoscope provides position information of the electron. This information is used for checks and corrections only.

A Møller electron pair is defined as a coincidence between the left and right lead-glass detector. Møller electrons separated 43 to 55 cm from the beam-line – corresponding to 83° to 97° scattering angle – are accepted. The detector acceptances are optimized for minimum coincidence loss, a small Levchuk effect (see 5.3) and a maximum count rate (chapter 5).

The lead glass shower counters provide accurate timing and energy information. To obtain a good energy resolution requires the physical lead glass area to be about one Molliere radius larger in width than the sensitive area. The acceptance is defined by collimators placed directly in front of the detectors. To be less dependent on small mistunings in beam or magnet settings one detector collimator is made larger. A small mistuning is no more leading to a coincidence loss and cancels out to first order.

A hodoscope is placed in front of the lead glass detectors and delivers position information of the electrons. The hodoscope is segmented in 14 horizontal channels (different CM scattering angle). Channels 3 and 12 are split vertically to provide some information on the vertical distribution. The horizontal resolution was chosen to be comparable to the FWHM of multiple scattering – the detectable lower limit.

The exact dimensions and acceptances of the Pb-glass and the hodoscope detectors are shown in the following Figure 2.7.

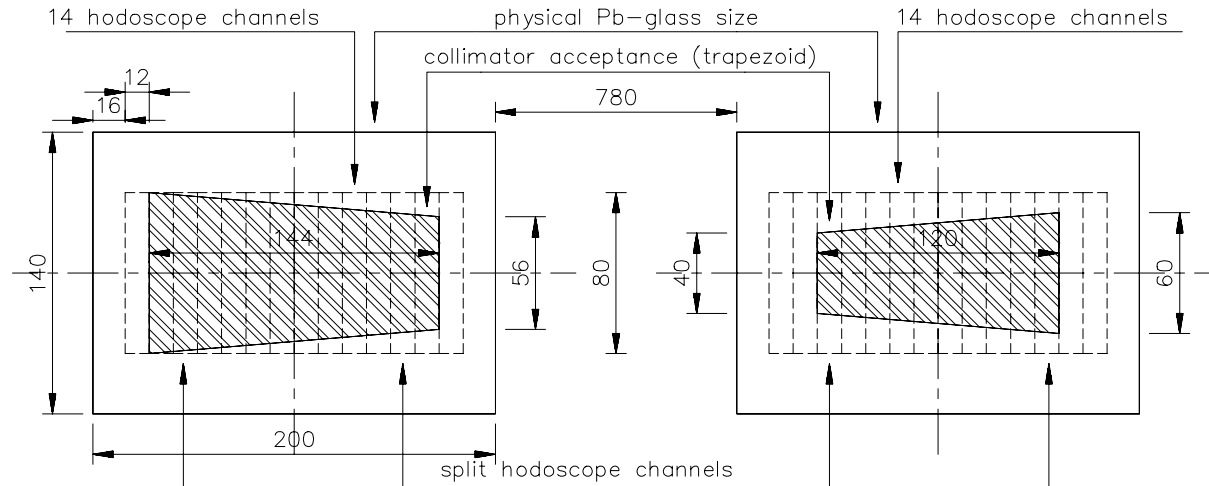


Figure 2.7: Actual sizes and acceptances of the detectors in mm. The two Hodoscopes consist of 14 channels each. Channel 3 and 12 are split. The Pb-glass detectors need, due to the process of showering, to be larger than the actual acceptances – both sizes are shown.

Materials used:

The main detectors consist of a SF2 Pb-glas block ($20\text{cm} \cdot 14\text{cm} \cdot 23\text{cm}$) from Schott. They are coupled with a thermo plastic (melt mount) to a Philips XP4512B 5 inch 10 stage photo multiplier (see Appendix D).

The hodoscopes are made from 8mm thick, 12mm wide and 80mm long BC 418 plastic scintillators which are glued directly to 8mm Hamamatsu R 1635 photo multipliers.

The distribution of coincidence events for the Pb-glass and the hodoscope detectors derived from the Monte Carlo simulation (Section 5), are shown in the following Figure 2.8.

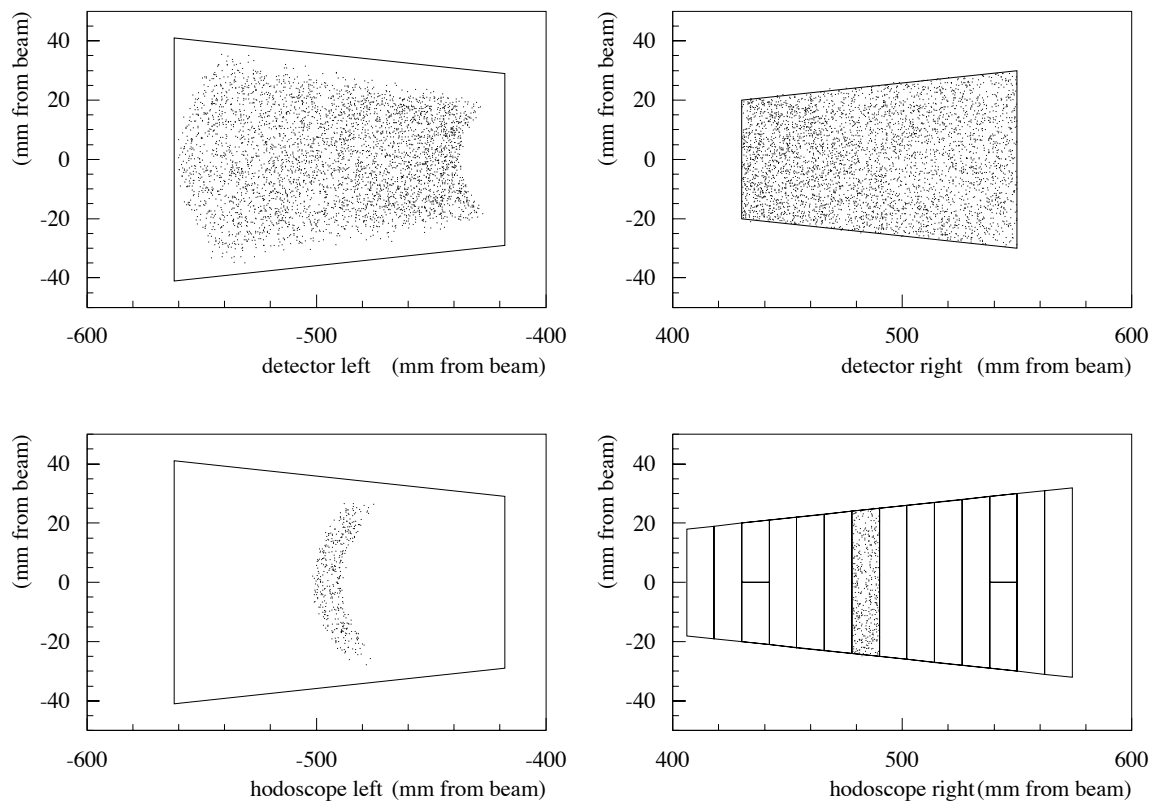


Figure 2.8: Monte Carlo simulation of events at the detectors. Upper right: active area of lead glass detector. Upper left: distribution of the corresponding coincident events. Lower right: example of one hodoscope channel. Lower left: distribution of the corresponding coincident events.

2.3 Electronics

An event is defined by a hardware coincidence between the two shower counters. This will trigger the two-ECL discriminators and the fast memories in order to get the hodoscope hit pattern. The logic diagram of this setup is shown in Figure 2.9. As the energy of the two Møller electrons always adds up to exactly the beam energy, we could make use of that by summing the two signals and discriminating on the sum – another possibility for the main trigger.

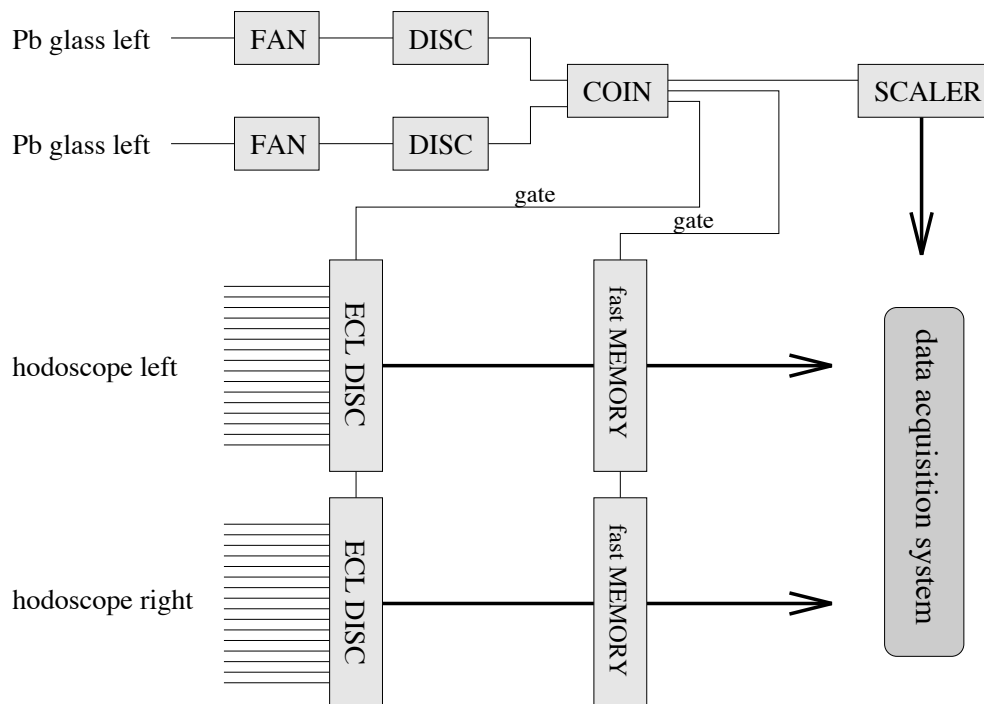


Figure 2.9: Logic setup of the electronics: The hodoscope part is only used for checks or verifications (e.g. alignment, quadrupole settings, Levchuk effect).

As the count rate is too high for an event by event read out, the shower counter coincidences are accumulated in a scaler. The position information derived from the hodoscopes is recorded in two fast memories which are read out after every 16K events. The two-dimensional graph of hits in the hodoscope channels of the left versus the right arm should show a diagonal ridge. Events at lower CM angle in one hodoscope should occur at higher CM angle in the other hodoscope. The expected pattern for correct optics is shown in Figure 2.10.

Standard electronics required for the shower counters:

2 fans, 2 discriminators and 2 quad majority logic units all NIM standard, which will fit in a CAMAC crate via an adapter. The shower counter electronics allow a maximum rate of 150 MHz at the coincidence, which is far above the maximal expected rate of a few MHz, so dead time due to electronics should be small.

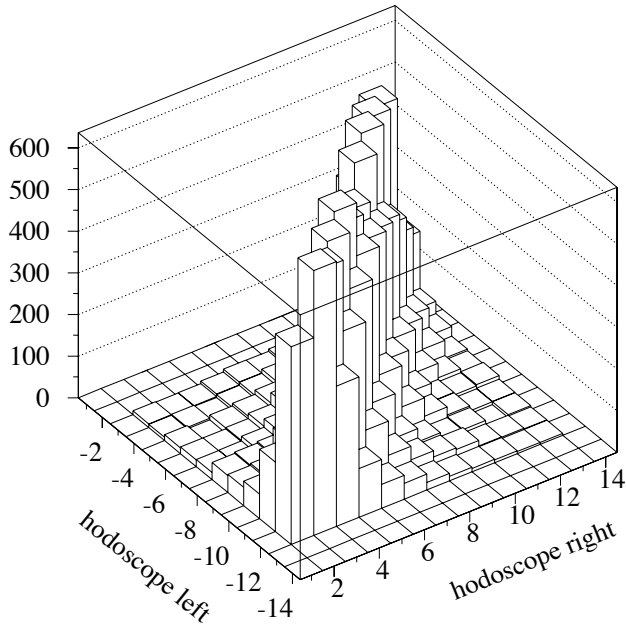


Figure 2.10: The expected distribution of events in the hodoscopes for an optimal tuning. Shown is the hit pattern of the right hodoscope versus the left hodoscope

2	Philips	model 740	quad linear fan-in/fan-out
2	Philips	model 704	quad discriminator
2	LeCroy	model 365 AL	quad majority logic unit
2	LeCroy	model 2551	12 chan. 24-Bit scaler

Table 2.2: NIM units

Standard electronics required for the hodoscope part:

We use the following ECL electronics: gated LeCroy discriminators and a LeCroy fast memory which can stack 16K 16 bit words. The hodoscope electronics can operate at a rate of 10 MHz which is limited by the speed of the fast memories. These electronics are dead for a few 100 ms during the read out cycle of the fast memories. The hodoscopes will only be used to check the whole system adjustment. The units purchased are listed below:

3	LeCroy	model 4413 AL	16 chan. updating discriminator
3	LeCroy	model 4302	triple port fast memory FERA

Table 2.3: CAMAC-ECL units

Chapter 3

The Møller target

All Møller targets presently used lead to relatively high uncertainties due to the poor knowledge of their magnetization ¹, as the low B-fields applied do not completely 'saturate' the foil. For many target materials the relation between magnetization (the observable) and the spin polarization (the quantity of interest) is not that well known. An additional disadvantage is the fact, that depolarization due to heat (resulting from high currents) remains undetected. To address this problem, alternative target-setups were evaluated by S. Robinson [Ro94]. Driving the foil magnetization into saturation with a high B-field should lead to a good absolute knowledge of the magnetization. An online survey of the target magnetization with a laser system will allow to correct for demagnetization at high beam currents.

3.1 Different ways of magnetizing

The common way of magnetizing Møller targets is based on in-plane magnetization, which is cheap and easy to realize. A pair of Helmholtz coils produces a small magnetic field with a strength of the order of 0.01 Tesla. A ferromagnetic foil, which is mounted under a small angle with respect to the beam, is magnetized in foil direction, see Figure 3.1.

Disadvantages of *in-plane* magnetization are:

- The field is too small to induce a complete saturation, hence the magnetization has to be measured with pick-up coils.
- The absolute calibration in an electron beam environment is difficult.
- Thickness inhomogenities lead to errors in the relation between magnetization and measured flux change.
- Demagnetization due to heat remains undetected.

¹In theory of magnetism the expression magnetization density is used, which is related linearly with the electron polarization of the ferro-magnetic material.

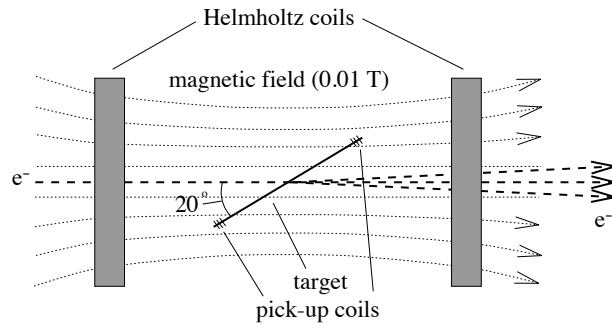


Figure 3.1: In-plane target: uses pick-up coils to measure the magnetization.

- The materials used need a small in-plane saturation value, which restricts the choice to iron alloys. Their relation between spin-polarization and magnetization is known far less accurately than for pure iron.

In contrast, the out-of-plane method uses a strong magnetic field (4 Tesla) which allows to polarize in the direction perpendicular to the foil plane, Figure 3.2. This setup allows an online survey with a laser beam using the polar Kerr effect. The only draw back is the expensive super-conducting magnet needed to produce such high magnetic fields.

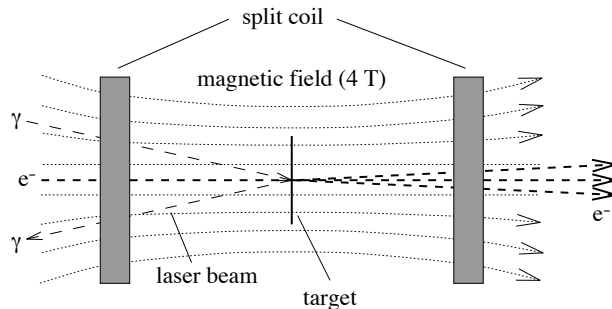


Figure 3.2: Out-of-plane target: uses reflected laser light to verify that the target is saturated.

Advantages of *out-of-plane* magnetization are:

- We can rely on a complete saturation. No absolute calibration is necessary.
- Variations in thickness are unimportant.
- Demagnetization due to heat is detectable.
- Iron, with the most accurately known relation between spin-polarization and magnetization, can be used.

3.2 Precise saturation values for our application

For the fully saturated target we need to know the exact number of electrons per atom which are aligned parallel to the field, M_{spin} [μ_B per atom]. To get the target electron spin-polarization M_{spin} we need M_s and g' for this specific ferromagnetic material [Ro94].

The saturation magnetization M_s of a material is defined as the magnetization density at temperature $T \rightarrow 0K$ and external field $\vec{B} \rightarrow 0T$. However our experimental setup is neither at a temperature of $0K$ nor at a very small B-field and we need to correct for that. The relevant effects are listed below and discussed in more detail later (see 3.2.1):

- An increase in temperature results in a decreases of the saturation magnetization (see 3.2.1). The process is caused by the temperature motion which constantly tries to misalign electrons (-2%).
- A large external B-field (e.g. 4 Tesla) results in an increase of the saturation magnetization (see 3.2.3). To some extend strong B-fields realign electrons which are misaligned due to the temperature motion and additionally align electrons usually responsible for the paramagnetism ($+0.5\%$).
- A misalignment of our out-of-plane target results in an in-plane contribution of the magnetization. This lowers the relevant magnetization in the beam direction (see 3.2.2). The effect should stay small which can be verified by the shape of the saturation curves, see Figure 4.6 (maximal contribution -0.1%).

These corrections have been calculated for room temperature (20^0C) and a B-field of 4 Tesla ². To get the target electron spin-polarization we need to subtract the contribution due to the orbital momentum (M_{orb}) from the saturation value M_s and divide the result (M_{spin}) through the total number of electrons per atom (26 for pure iron)[Ro94]. The final target electron polarization for the CEBAF Møller target is given in Table 3.1.

Effect	M [μ_B]	error	reference
saturation magnetization $M_s(T \rightarrow 0K, B \rightarrow 0T)$	2.2160	± 0.0008	[Da68]
saturation magnetization $M_s(T=294K, B=1T)$	2.177	± 0.002	[Gr82]
corrections for $B=1 \rightarrow 4T$	0.0059	± 0.0002	[Pa82]
saturation magnetization $M_s(T=294K, B=4T)$	2.183	± 0.002	
magnetization from orbit (M_{orb})	0.0918	± 0.0033	[Re69]
remaining magnetization from spin M_{spin}	2.0911	± 0.004	
target electron polarization, $\frac{M_{spin}}{26}$ (T=294K, B=4T)	0.08043	± 0.00015	

Table 3.1: Magnetization/polarization values for the out-of-plane target. M_s : Saturation magnetization: μ_B (Bohr magnetons) per atom.

Further explanations are given in the following sections or the references.

²the demagnetization due to target misalignments has been neglected for the moment. A correction would have to be done by fitting saturation curves (Figure 4.6) with simulations (Figure 3.5), individually for every saturation.

3.2.1 Ferromagnetism: temperature dependence and domain structure

Ferromagnetic materials acquire a large magnetization in relatively small magnetic fields. This magnetization corresponds to all atomic magnetic moments being aligned. For fields of the order of a few Tesla, at room temperature, most ferromagnetic materials would be saturated. Many of them would be saturated in fields very much less than 1 Tesla.

The value of the saturation magnetization varies with the temperature, T , decreasing from a maximum value at $T = 0K$ at first slowly, then more and more rapidly as T increases, becoming zero at the Curie temperature, Θ_C (for Fe: 1017 K). For temperatures $T \ll \Theta_C$ this behavior is roughly described by the following Equation [Bl30]

$$M_s(T) = M_s(T = 0K)(1 - a_{\frac{3}{2}}T^{\frac{3}{2}}), \quad (3.1)$$

where M_s is the saturation magnetization and $a_{\frac{3}{2}}$ constant for a given material. Higher terms in T do improve the agreement for temperatures closer to Θ_c . For an accurate temperature dependence one must rely on experimentally measured values as no theory accurately agrees with the experimental data points, Figure 3.3

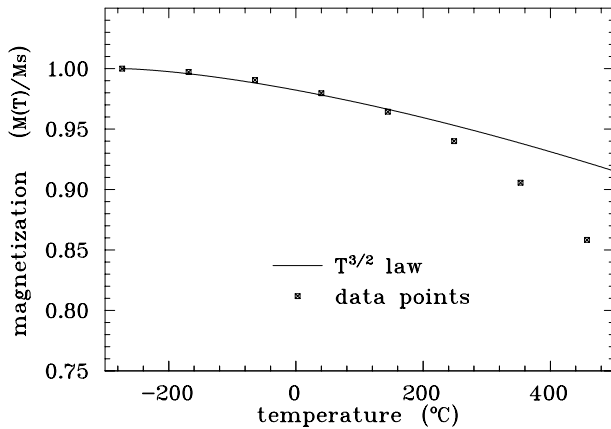


Figure 3.3: Comparison of experimental data and the $T^{\frac{3}{2}}$ law. The agreement is fairly poor - higher terms in T do improve the agreement for temperatures closer to Θ_c .

At temperatures higher than Θ_c the behavior is similar to that of paramagnetic materials, with the magnetization being proportional to the field.

The behavior outlined so far suggests that in ferromagnetic materials, the atomic magnetic moments have a strong tendency to be aligned parallel to each other. This tendency aids the external field in producing saturation. In order to explain these effects Weiss introduced the concept of *magnetic domains*. He postulated that a ferromagnet is divided into regions (domains), within which the magnetization is equal to the saturation value. The magnetization of different domains points in different directions, so that the magnetization of a ferromagnetic specimen could be small or even zero. An external field can then align the domains such that a macroscopic magnetization results. The external field needed for a complete alignment (saturation) is dependent on the shape and the orientation of the ferromagnet in the applied field. The maximal value is of the order of the field inside a domain – the saturation value.

3.2.2 Out of plane magnetization

When the physical size of a magnetized body is made smaller, the relative contribution of the domain boundary energy to the total energy increases. Eventually a point is reached where it is energetically unfavourable for a domain boundary to be formed. The specimen then behaves as a single domain and its properties differ from the properties when domain walls are present.

Such situations occur in heterogeneous magnetic alloys where small ferromagnetic particles are dispersed in a non-ferromagnetic matrix. It turns out that magnetizing a thin foil perpendicular to its plane can be treated in exactly the same way. The relevant size, the foil thickness, is small and the domain boundary energy is energetically very high.

The self energy η is given by

$$\frac{\partial \eta}{\partial \phi} = \frac{1}{2} \sin 2(\phi - \theta) + B \sin \phi = 0, \quad (3.2)$$

where B is the applied field, θ the angle between the foil plane and the B -field, and ϕ the angle between the magnetization and the B -field. For fixed B and θ it can be solved for ϕ numerically [Cr91]. Solutions of Equation 3.2 are required which give equilibrium values for ϕ over a range of values for B at different values of the orientation. The term $\cos \phi$ then reflects the magnetization in the field direction. Graphs of solutions for different values of θ are shown in Figure 3.4.

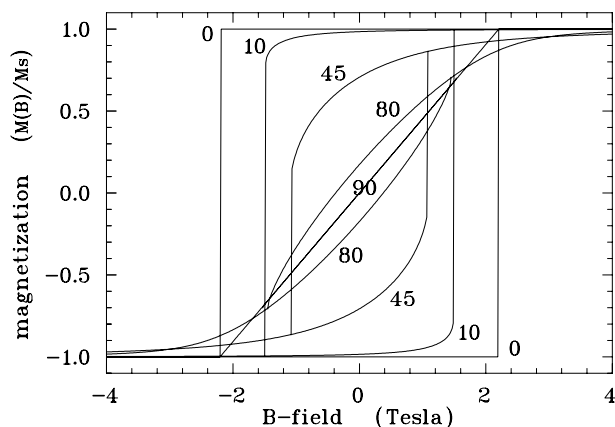


Figure 3.4: Simulation for different angles between the foil plane and the B-field direction. 0 degrees corresponds to in-plane, 90 degrees to out-of-plane. $M(B)/M_s$ is the cosine of the solutions $\phi(B, \theta)$.

A more detailed simulation for angles close to 90° , the relevant region for our situation, is shown in Figure 3.5.

Controlling the angle of the Møller target can be done to better than 0.5° but the resulting warp of the target has to be observed carefully. The warp has been estimated to be smaller than 2° ³ (88° out of plane) the resulting error in the magnetization is smaller than 0.1% which is consistent with the measured curves.

³A warp could be caused by the ultra strong B-field or the thermal expansion at high beam currents. Estimations can be made by observing the change in angle of the reflected laser beam.

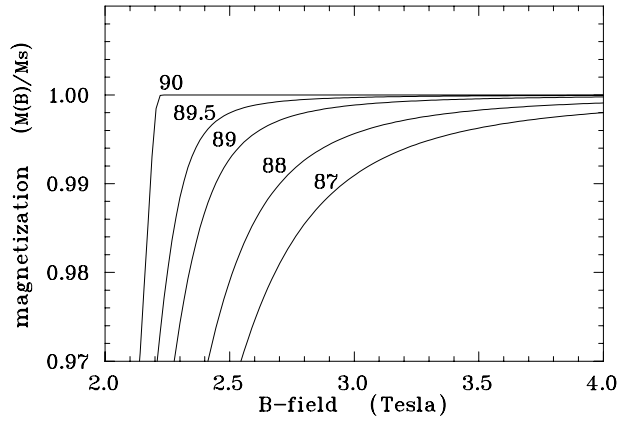


Figure 3.5: Simulations for angles between the foil plane and the B-field direction close to 90 degrees. Errors due to imperfect alignment or a slight warp of the foil could produce such a result.

3.2.3 Correction terms for strong B-fields

The effective magnetization of a ferromagnetic sample when saturated is the saturation or spontaneous magnetization, M_s . This is only accurate for long thin probes, temperatures close to absolute zero and small applied fields. The effect of the temperature and the geometry has been discussed before. Using strong magnetic fields, two correction terms are required [Pa82].

- The spin wave term: action of the magnetic field on the spin waves, proportional to \sqrt{B} (vanishes at zero temperature).
- The high field term: response of the conduction electrons, proportional to B .

Both terms are positive and raise the final magnetization value. The absolute accuracy of the correction is better than 0.01% of the final magnetization. The resulting equation including these corrections is

$$M_s(B, T) = M_s(T) + a(T)B^{\frac{1}{2}} + b(T)B. \quad (3.3)$$

The pure B-field dependence is shown in Figure 3.6.

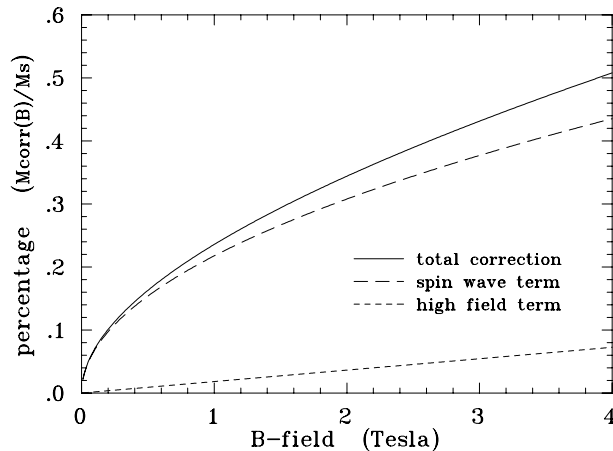


Figure 3.6: The contributions of the two correction terms for room temperature: 1.) The spinwave term, proportional to \sqrt{B} is only due to the non zero temperature. 2.) The high field term is the resultant of the 3d 4s electrons and the different diamagnetisms.

Chapter 4

Measuring magnetization with the Kerr effect

The magnetic saturation of the CEBAF Møller target is measured using the Kerr magneto-optic effect ¹ which in strength is proportional to the magnetization of the sample. Furthermore is the magnetization linearly related to the electron polarization which allows us to perform a relative measurement of the latter one using the Kerr magneto-optic effect.

The Kerr magneto-optic effect alters the polarization properties of the light scattered off of a magnetized sample. For a detailed theoretical explanation the reader is referred to the references ([Hu32], [La60], [Pe60], [Ze91] and [Ro94]). The various configurations of the orientation of the magnetization of the sample, the surface of the sample and the plane of incidence of the light lead to three classes of Kerr effects: the Polar, Longitudinal and Transverse Kerr effects [LB86]. Geometrical setup and out-of-plane magnetization of our target allow us to use the Polar Kerr effect (Figure 4.3), which is one order of magnitude larger than the Longitudinal or Transverse Kerr effect.

4.1 The Polar Kerr effect

The magnetization is perpendicular to the surface, parallel to the direction of the incident linearly polarized light: the polarization is rotated through an angle α_K given by

$$\alpha_K = K_R M \tag{4.1}$$

where K_R is the Polar Kerr constant and M the magnetization of the sample. A geometrical view of what happens to the polarization is given in Figure 4.3.

The rotation angle of the polarization depends on the kind of Kerr effect (polar, longitudinal or transverse), the material (iron, nickel, cobalt) and the wavelength of the scattered

¹named after the scottish physicist John Kerr (1824-1907), pronounced 'kar', who first observed this effect in 1888. Sometimes also referred to as MOKE, SMOKE.

light. For the polar Kerr effect and a saturated iron sample, rotation angle versus wave length is shown in Figure 4.1 [LB86].

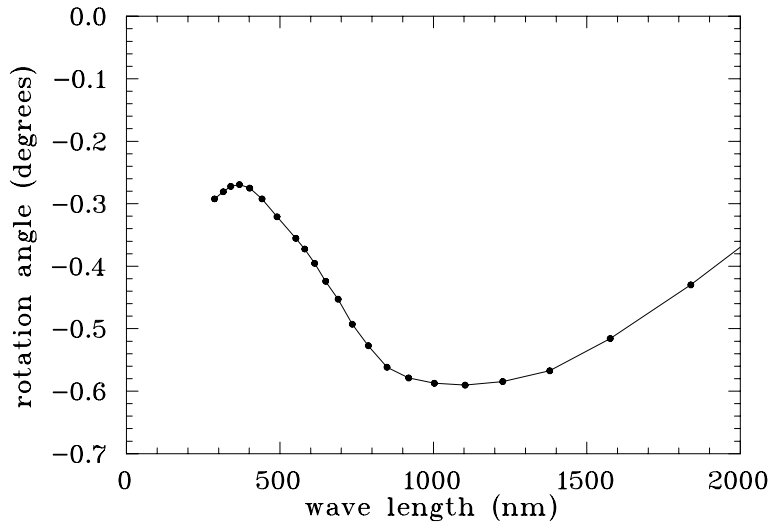


Figure 4.1: Polar Kerr effect: Rotation angle of the polarization as a function of wavelength of incident light quanta. The laser used in our apparatus has a wavelength of 690nm. The resulting angle of rotation for a saturated iron sample is approximately 0.45°

4.2 Setup of the Kerr apparatus

The setup of the Kerr system, as previously used by S. Robinson [Ro94], is shown in Figure 4.2.

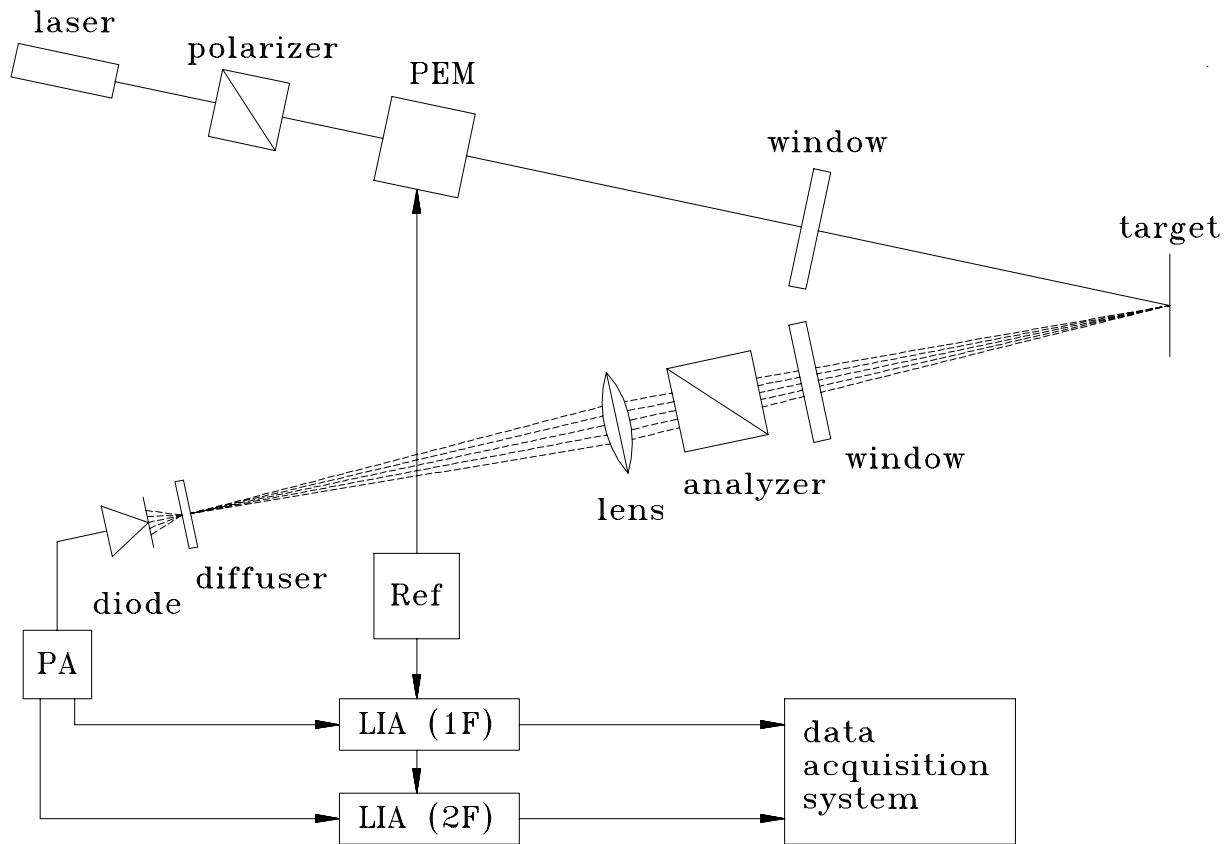


Figure 4.2: Setup of the Kerr apparatus. PEM: photo-elastic modulator, Ref: 50 kHz reference signal, PA: preamplifier, LIA: lock-in amplifiers.

First we polarize the laser beam vertically, then a PEM modulates the polarization direction² with 50 kHz by $\pm 30^\circ$. The modulated laser-beam now passes through a vacuum window and is reflected from the target (see Figure 4.3). As the surface of our iron foil is optically not perfect the reflection angle has a small dispersion. Exiting the vacuum through a second window and passing a horizontal polarizer (analyzer) we refocus the laser-beam on a diffuser and detect the intensity with a photodiode. By the second polarizer we project the polarization on the horizontal axis – this is the only signal we finally detect. The effect of the PEM on the polarization is shown in Figure 4.3.

²This is a simplified view. To understand fully what the PEM does one needs to introduce circular coordinates which lead to a modulation of the polarization direction and ellipticity [Ze91].

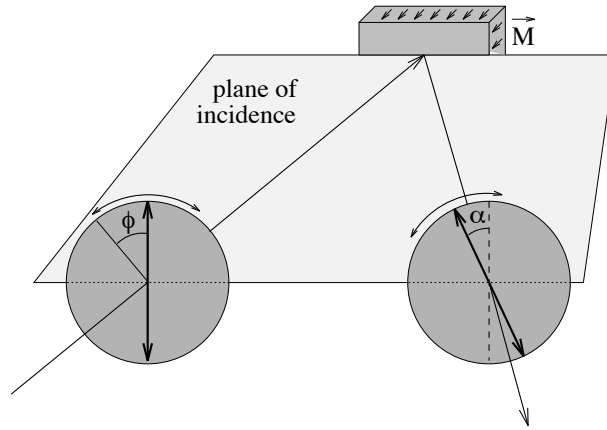


Figure 4.3: The incoming polarization is modulated by the PEM with the frequency ω , by the angle $\pm\phi$. The polarization of the reflection is, through the Kerr effect, rotated by the angle α . What we finally measure is the horizontal component of the polarization.

With turned-off PEM and an unmagnetized foil the light gets absorbed totally. Experimentally this is used to verify that the two polarizers are oriented at 90° with respect to each other. If we turn on the PEM a signal with twice the frequency of the PEM ($2F$) is detected. Magnetizing the target creates an additional small component with the frequency of the PEM ($1F$) which is proportional to the rotation due to the magnetization, Figure 4.4.

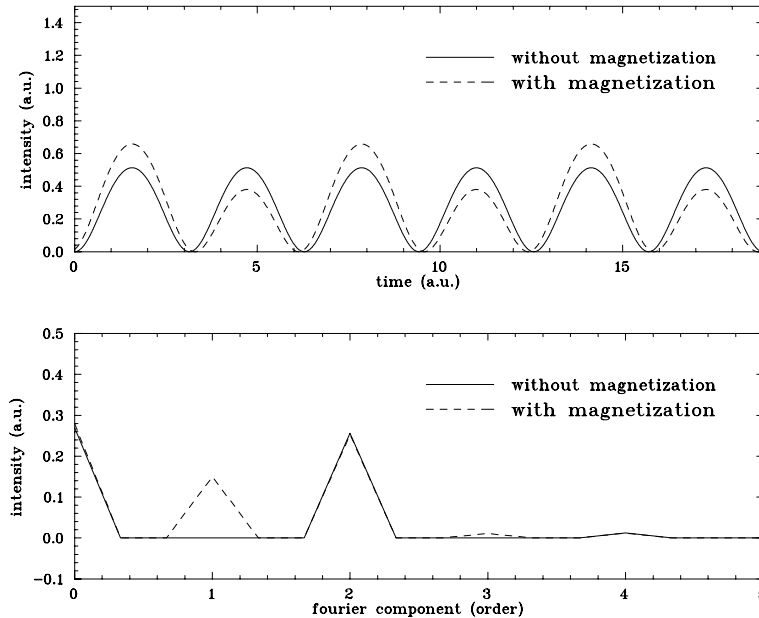


Figure 4.4: Signal change due to magnetization: The small rotation introduced by the Kerr effect caused the alternating growth/shrink of every second peak (upper graph). Comparing the fourier spectra of the two signals shows that magnetizing introduces an additional $1F$, $3F$, $5F$... component (lower graph). The effect is enlarged by a factor 10.

To measure these two signals we use lock-in amplifiers. Such an amplifier has two inputs, the AC-reference coming from the PEM and the signal coming from the preamplifier. The lock-in measures the intensity of the frequency component which matches the reference frequency. The $1F$ signal is proportional to the magnetization as well as to the reflected intensity, whereas the $2F$ signal is only proportional to the reflected intensity. The ratio $\frac{1F}{2F}$ is proportional to the magnetization and independent of any intensity changes.

4.3 Saturation measurements

With the setup described before (4.2) it is only possible to measure relative magnetization. In order to get a calibration point we need to verify that our sample is saturated; in saturation the magnetization is known very accurately. This is done by ramping up the magnetic field to a value larger than the saturation magnetization of the sample. As long as we are below the saturation value the magnetization measured with the Kerr apparatus increases linearly with the magnetic field applied (see Figure 3.4). At the point where the saturation is reached the magnetization of the sample stays at a constant value while the magnetic field increases further. Ramping down the field gives a symmetric result. A complete ramp up-down to 3 Tesla is shown in Figure 4.5.

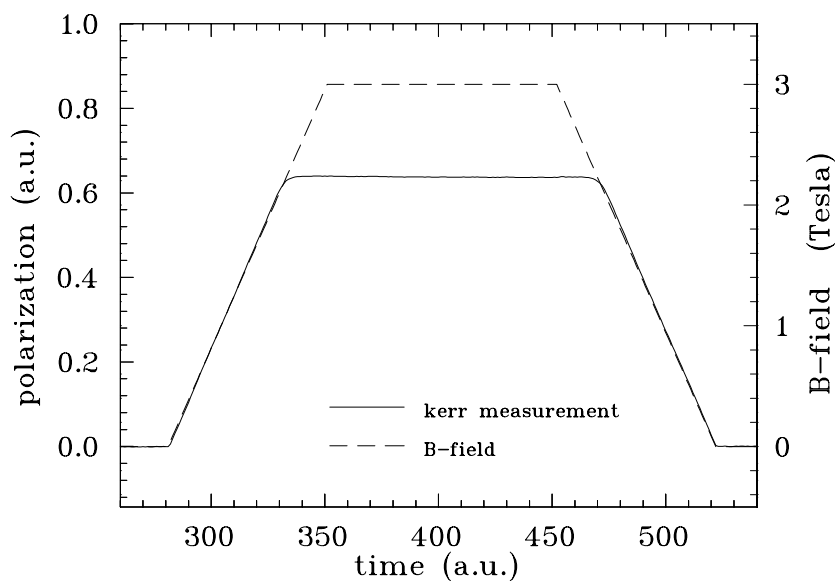


Figure 4.5: Kerr measurement: a complete ramp up-down to 3 Tesla. The kerr signal clearly saturates at 2.2 Tesla.

To estimate how accurately our sample is saturated we need to look a bit closer at the point where the saturation takes place and what happens by a further increase of the field. Enlarging this area, we can verify that our sample is fully saturated. The reasons for a less than complete saturation and the slight slope still present is discussed in chapter 3.2.2 and 3.2.3. The saturation point is shown in a plot displaying magnetization versus applied B-field, Figure 4.6.

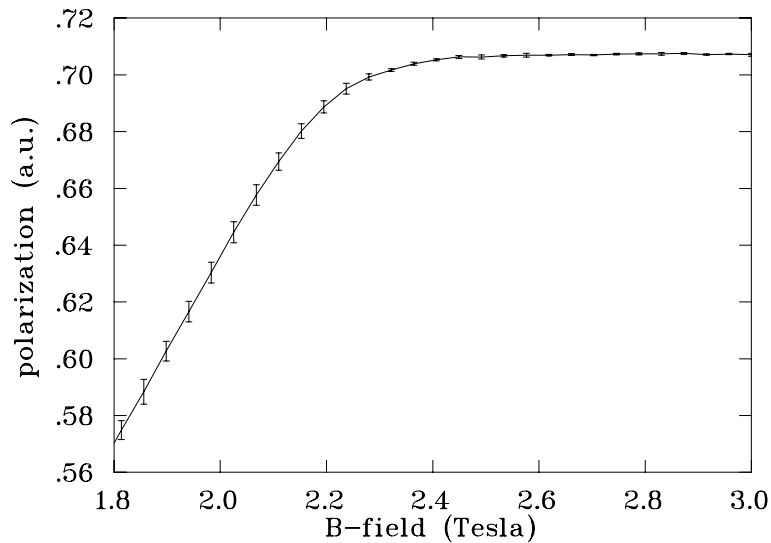


Figure 4.6: Saturation measurement: Magnetization as a function of applied B field. The saturation of our sample is clearly seen, the slow approach of the magnetization to the saturation value is explained in chapter 3.

4.4 Depolarization measurements

The main effect responsible for a depolarization during the experiment is a temperature rise. The electrons lose energy when passing through our iron target, this energy is converted nearly 100% in thermal energy and causes a temperature rise (for quantitative calculations see 4.5). To get a quantitative check we have measured this depolarization while heating the iron foil using the Kerr apparatus. This was done with the setup shown in Figure 4.7.

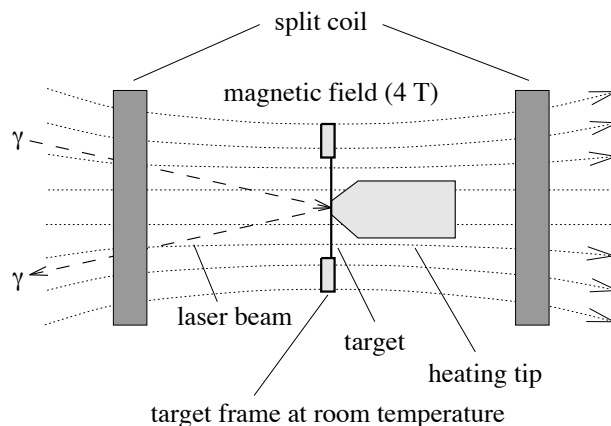


Figure 4.7: Depolarization setup: The target foil is heated from the back by a solid molybdenum tip equipped with a temperature sensor. The laser-beam for the Kerr measurement is reflected from the opposite side of the foil. With this setup we could reach temperatures up to 600°C . However reliable measurements were possible up to 250°C only.

In these tests we heated the iron foil to a certain temperature and let it cool down after that. The Kerr signal was verified to come back to its initial value which ensured that no permanent change in the reflecting properties of the foil took place. The maximal temperature was increased from cycle to cycle to find the point where we either permanently change or damage the foils Kerr properties. Above 300°C the Kerr signal did not come back to its initial value. This indicates that the foil surface has been changed and Kerr measurements are no more reliable in these temperature regions. Cycles below 300°C are shown in Figure 4.8.

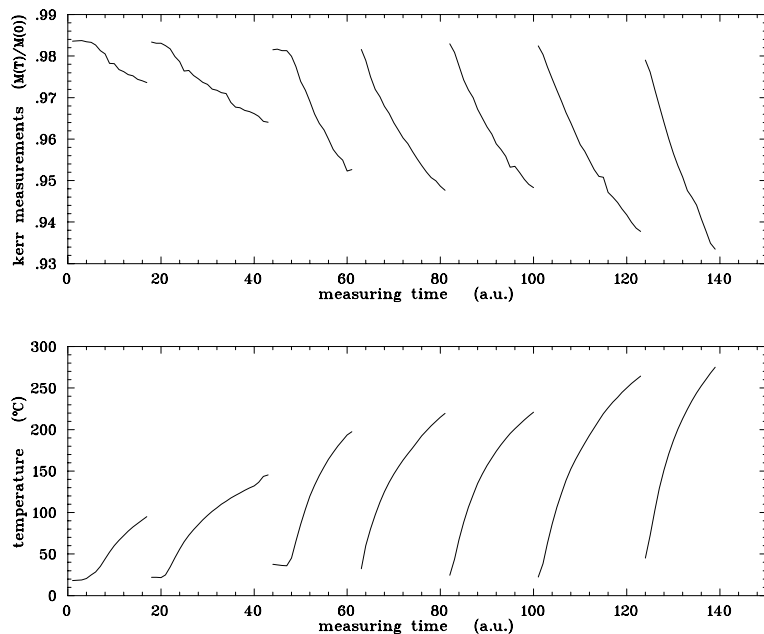


Figure 4.8: Depolarization due to rising temperature: The top panel shows the relative Kerr signal for 8 different heating cycles, the bottom panel shows the corresponding temperature increase. A heating cycle approximately took 2 minutes.

If we now analyze these data by comparing the measured depolarization with the applied temperature a plot of temperature versus polarization results, Figure 4.9. All 8 heating cycles show a similar behavior and match the slope of the world data curve. Data are accurate up to 250°C within 0.25%. Up to 300°C the accuracy gets worse and above that, Kerr measurements are no more possible, as irreversible deformations occur. Data taken below 300°C are shown in Figure 4.9.

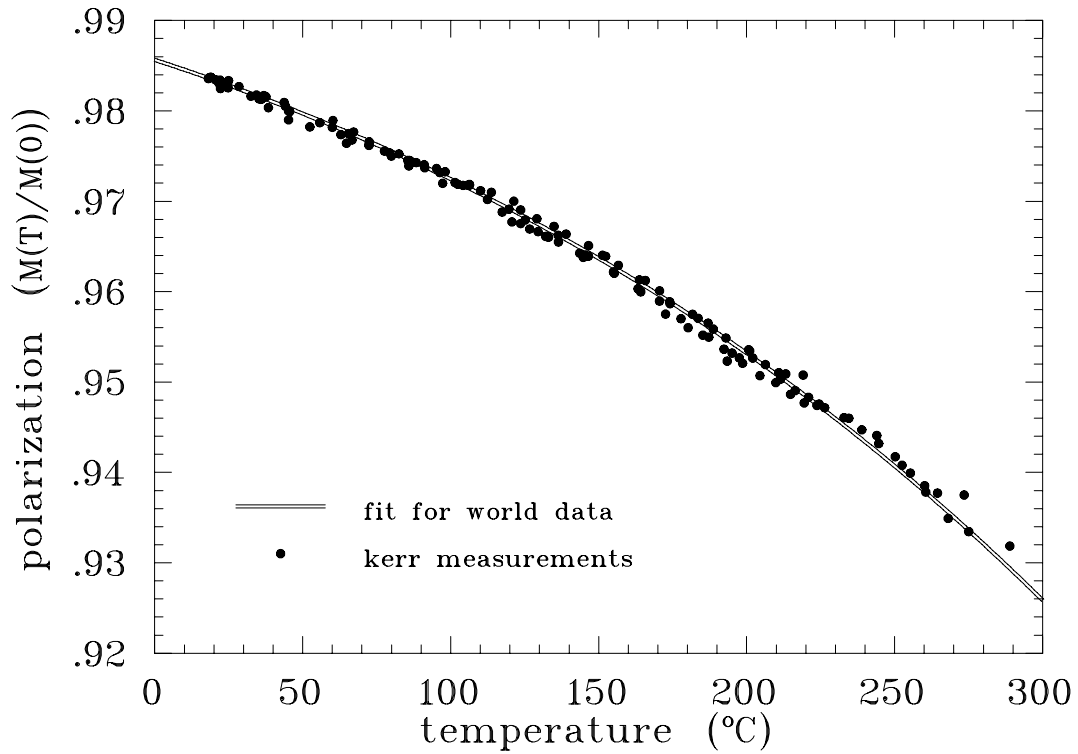


Figure 4.9: Depolarization measurements with the Kerr apparatus show that the measured depolarizations agree with known saturation data. The error up to 250⁰C is better than 0.25% . For higher temperatures the thermal expansion of the iron foil is too large and produces a strong warp which causes problems with the reflection of the laser beam.

4.5 Power deposition in the target

An electron beam with a small diameter, e.g. a few 100 μm , produces a large local power deposition in the target. Currents higher than a few μA cause a significant local temperature rise. The heating of a stationary round target was estimated with the following equation [Ge86]:

$$\Delta T = \frac{Q}{2} \frac{I}{\pi \lambda_{Fe}} (\ln(R_{target}) - \ln(R_{beam})). \quad (4.2)$$

Q = energy deposition for an iron target [$1500 \frac{W}{\mu A \cdot m}$] (used energy loss: $2 \frac{MeV}{g \cdot cm^2}$)

I = beam current [μA] λ_{Fe} = thermal conductivity of iron [$\frac{W}{m \cdot K}$]

R = radius of beam spot / target frame [m]

The relation between the beam radius and the temperature is shown in figure 4.10.

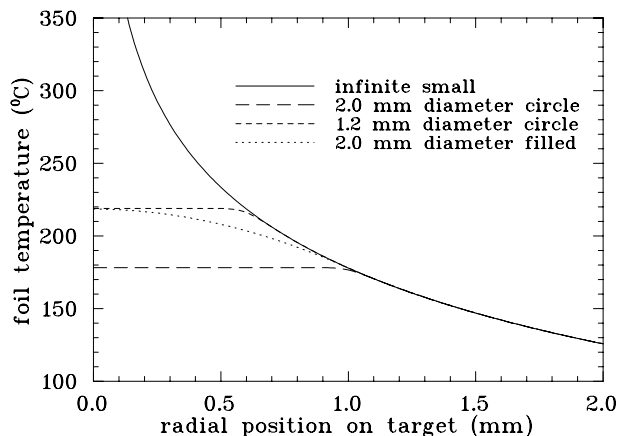


Figure 4.10: Beam spot temperature as a function of beam radius. Conditions of the simulation were: a round 2 cm diameter iron target with a solid frame at room temperature and $20 \mu A$ beam. For the numerical calculation equation 4.2 was iterated using a temperature dependent thermal conductivity.

The corresponding target magnetization distributions of the beam-spots used in Figure 4.10 are shown in the following Figure.

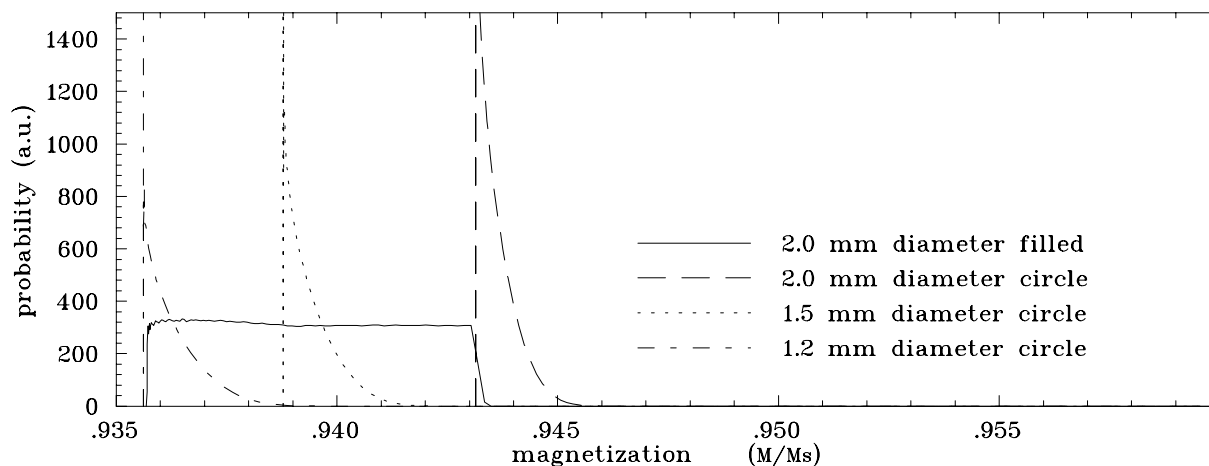


Figure 4.11: Magnetization deviations for different beam-spot shapes. A filled beam-spot has the same average polarization like a 25 % smaller circular beam-spot.

The rise in temperature causes a polarization loss (see 3.2.1, Figure 3.3). At the Curie temperature Θ_c (770°C) the polarizability of iron vanishes, therefore any useful polarization measurement requires temperatures far below Θ_c . The relation between beam-current and polarization is shown Figure 4.12.

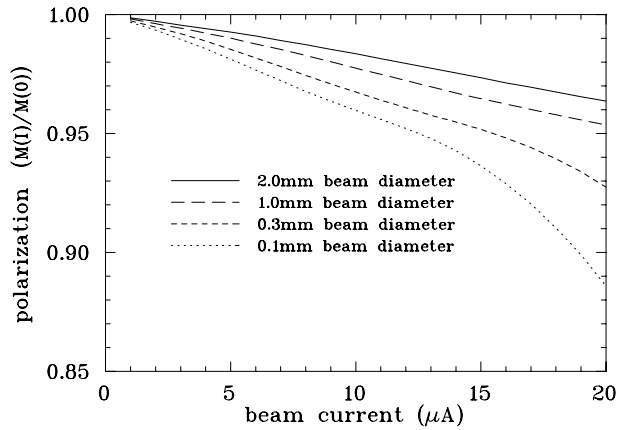


Figure 4.12: Relative polarization as a function of beam current. For varying beam currents the results were taken from Figure 4.10 . For high beam currents the polarization starts to depend strongly on the beam radius. Therefore one needs to avoid small beam spots.

For beam currents higher than $20\mu\text{A}$ the setup therefore will involve a rotating target or a target foil with a differential thickness (thin center and thick outer part). Both methods will allow to transport more heat and therefore allow for higher beam-currents.

Chapter 5

Monte Carlo Simulations

When considering Møller scattering there are three secondary effects which have to be taken into account. These are background contributions (mainly Mott scattering, 5.1), the momenta of the target electrons (Levchuk effect, 5.3) and multiple scattering (5.2). To get the final A_{zz} (see equation 1.2) of our polarimeter all these effects have been calculated using the Monte Carlo technique.

5.1 Mott background

The process of electrons scattering off of a nucleus of an atom is called Mott scattering. As we are only interested in the Møller electrons (electrons scattered off electrons) we need to estimate the contribution of these 'Mott electrons'. For a particular acceptance we can vary the ratio between the ϕ and the θ acceptance. The influence of this ratio on the amount of Mott background was studied using the program Radtail [RT81]. The conclusion from this simulation is, that the signal to noise ratio is inversely proportional to the theta acceptance, see Figure 5.1.

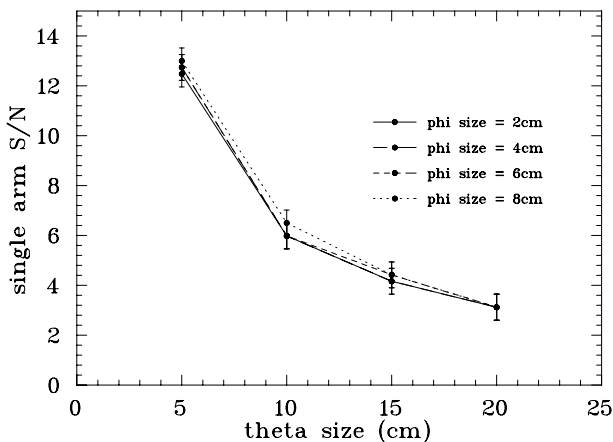


Figure 5.1: *Single arm* signal to noise ratio, Møller divided by Mott. An exponential θ dependence is observed whereas the ϕ acceptance has no influence on the signal to noise ratio. The coincidence condition will of course lead to a tremendous improvement.

The conclusion from this graph would be that it is advantageous to use a theta acceptance as small as possible. However other effects discussed later (5.2 and 5.3) require a moderate theta acceptance.

5.2 Multiple scattering

There are three different types of multiple scattering (labeled MS below). The calculations below have been done for a 20 μm thick iron target and scale with $\sqrt{\text{target thickness}}$.

- The multiple scattering of an electron before the Møller scattering process (estimated using half the target thickness). This effect is **correlated** because both Møller-electrons subsequently produced are deflected in the same way.
- The Multiple scattering of either or both Møller electrons after the Møller scattering process (**uncorrelated**). For the detectors $\sqrt{MS_{left}^2 + MS_{right}^2}$ is the important value.
- The Multiple scattering of the beam due to the Møller target (not relevant for the detectors).

The multiple scattering has been calculated with the following formula [PP86], which is accurate within 5 %.

$$\Theta_{ms-proj} = \frac{14.1 \text{ MeV}/c}{p \beta} z \sqrt{\frac{L}{L_{rad}}} \left(1 + \frac{1}{9} \log_{10} \left(\frac{L}{L_{rad}}\right)\right)$$

$\Theta_{ms-proj}$ = multiple scattering angle projected on x-direction

p = momentum of the electron

$\beta = \frac{v}{c} \simeq 1$

z = charge number of the electron

$\frac{L}{L_{rad}}$ = thickness of the target in radiation lengths (for 20 μ Fe: 0.0011)

E beam	90 ⁰ Møllers	MS-beam	MS-corr.	MS-uncorr.	MS at hodoscope
1.0 GeV	31.9 mr	0.453 mr	0.304 mr	0.860 mr	0.94 cm
2.0 GeV	22.6 mr	0.226 mr	0.153 mr	0.430 mr	0.67 cm
3.0 GeV	18.5 mr	0.151 mr	0.102 mr	0.287 mr	0.54 cm
4.0 GeV	16.0 mr	0.113 mr	0.076 mr	0.215 mr	0.48 cm
5.0 GeV	14.3 mr	0.091 mr	0.061 mr	0.173 mr	0.42 cm
6.0 GeV	13.1 mr	0.075 mr	0.051 mr	0.143 mr	0.37 cm

Table 5.1: Møller lab angle and multiple scattering for different beam energies.

In the table above are listed the unprojected angles, for an axial symmetric beam they correspond to $\approx \sqrt{2}$ times the projected multiple scattering angles. For the multiple scattering at the hodoscope, the projected RMS radius for the x-direction is listed.

The multiple scattering at the detector location is shown in Figure 5.2, the one of the beam in Figure 5.3.

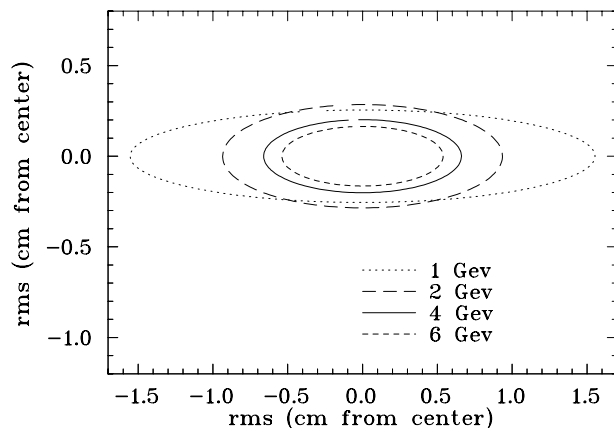


Figure 5.2: Multiple scattering at the detector plane, the RMS radius shown in 2D. Relevant for the hodoscope is the horizontal projection ($\langle \rangle_{proj,x}$), which is $\approx \frac{1}{\sqrt{2}} \cdot \langle \rangle_x$ [PP86].

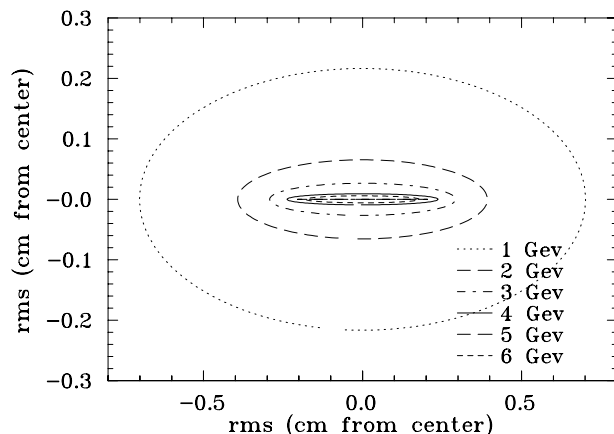


Figure 5.3: Multiple scattering of the passing beam 11 meters downstream of the Møller target where the next quadrupole is situated, shown for a $20\mu\text{m}$ iron foil. For high energies and a thin foil online polarization measurement might be possible.

Polarization measurements while physics experiments are going on might be possible. Table 5.2 shows the fraction of beam which is lost due to multiple scattering caused by the Møller target. For the multiple scattering a gaussian distribution was assumed.

E beam	σ accepted ($20\mu\text{m}$)	loss for $20\mu\text{m}$ target	$5\mu\text{m}$ target	$1\mu\text{m}$ target
1.0 GeV	1.6	0.11	0.0023	$< 1\text{E-9}$
2.0 GeV	3.0	0.044	$< 1\text{E-9}$	$< 1\text{E-9}$
3.0 GeV	4.0	1.3E-4	$< 1\text{E-9}$	$< 1\text{E-9}$
4.0 GeV	5.0	1.4E-6	$< 1\text{E-9}$	$< 1\text{E-9}$
5.0 GeV	5.8	3.5E-8	$< 1\text{E-9}$	$< 1\text{E-9}$
6.0 GeV	6.7	$< 1\text{E-9}$	$< 1\text{E-9}$	$< 1\text{E-9}$

Table 5.2: Fraction of the beam which is lost due to multiple scattering into the beam pipe. The simulation was done using a one inch beam pipe diameter after the polarimeter and a Gaussian multiple scattering distribution.

5.3 Levchuk effect

Only recently L.G. Levchuk realized that the asymmetries measured in Møller scattering polarimeters could be significantly affected by the intrinsic momenta of the target electrons. The asymmetries of the MIT-Bates polarimeter were reestimated and an increase by 5 – 10% was found [Le94].

The size of the effect is mainly dependent on the angular acceptance of the detectors in terms of degrees CM. The Levchuk effect can be corrected for using Monte Carlo simulations if the atomic momentum distributions are known. For the CEBAF Møller polarimeter we modified the Montecarlo which was used to simulate the SLAC single and double arm polarimeter [Sw95].

Simulations for the whole detector plane show, that the Levchuk effect causes an additional broadening of the distribution, Figure 5.4. Radiative losses, thick target Bremsstrahlung and multiple scattering with Moliere tails were taken into account.

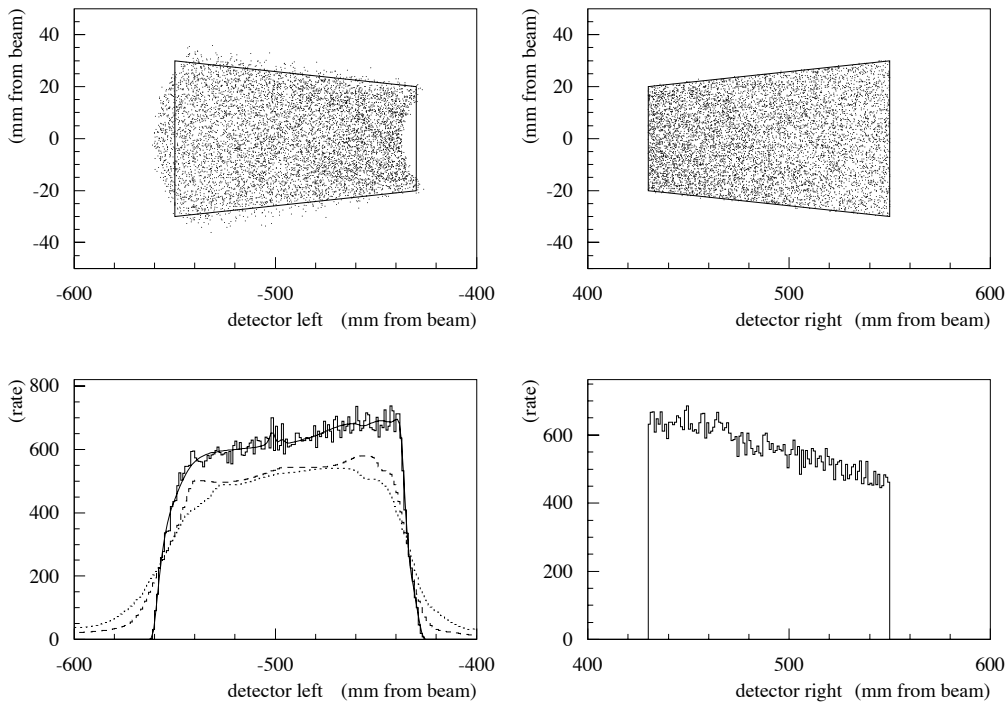


Figure 5.4: Monte Carlo simulation: Upper right: accepted events in the right detector. Upper left: resulting events in the left detector. Lower right: events projected on horizontal axis. Lower left: events projected on horizontal axis; only optics (solid), all effects excluding Levchuk (dashed) and all effects including Levchuk (dotted).

To provide a check of the tuning of magnetic elements and beam the hodoscope (see Chapter 2) will deliver us information. A single hodoscope channel with its coincidence events is shown in Figure 5.5.

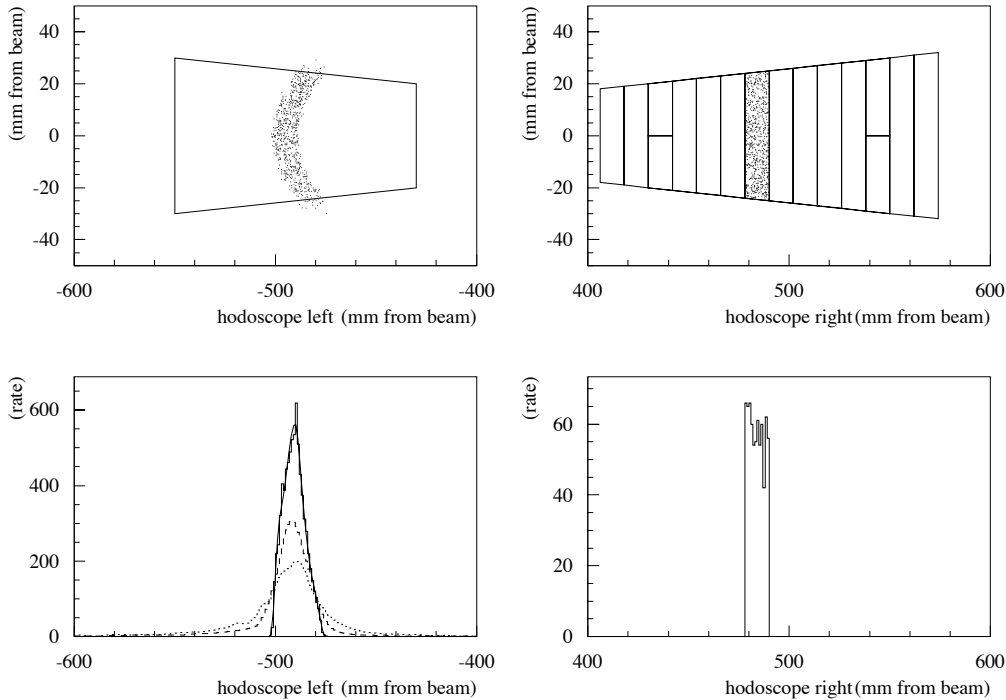


Figure 5.5: Monte Carlo simulation: Upper right: accepted events in one of the right hodoscope channels. Upper left: resulting events in the left hodoscope area. Lower right: events projected on horizontal axis. Lower left: events projected on horizontal axis; only optics (solid), all effects excluding Levchuk (dashed) and all effects including Levchuk (dotted).

If we require an event in one lead glass detector, events of the corresponding coincidence detector can be analyzed for their spatial A_{zz} distribution (Figure 5.6 and 5.7). The distribution over the coincidence detector shows a higher analyzing power A_{zz} in the central channels and a significantly smaller one at the edges. This is due to the fact, that the unpolarized electrons have in general higher binding energies i.e. high momenta; as a consequence the distribution of the corresponding Møller electrons gets broadened more. For a given acceptance the coincidence partners of unpolarized electrons are more likely to be outside, which leads to a higher A_{zz} (Figure 5.6). This however is only true for the CM (theta) direction, the phi direction shows a constant A_{zz} .

To avoid this problem one could make the coincidence detector much larger, such that all coincidence events get accepted. This is of course not realistic and introduces other problems, like a large background and countrate. Nevertheless making one detector slightly larger reduces the sensitivity to the Levchuk effect besides other advantages (see Appendix A).

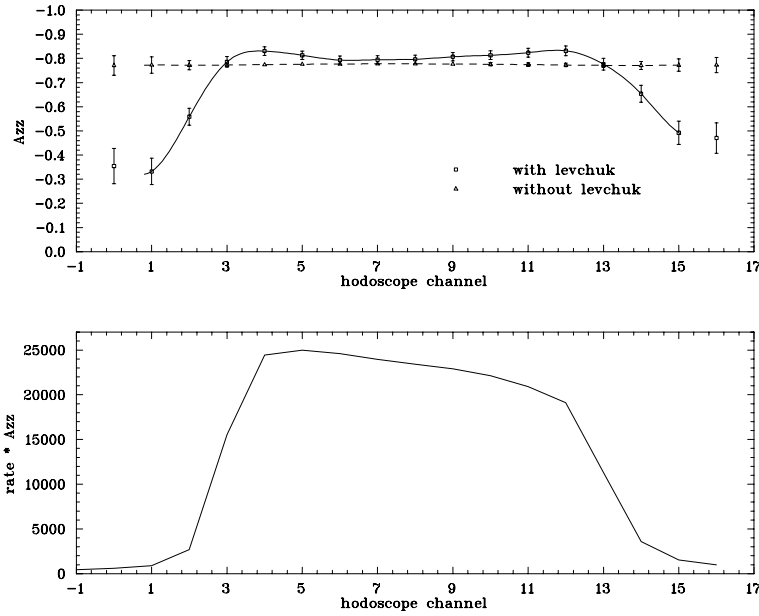


Figure 5.6: Monte Carlo simulation: Upper: A_{zz} as a function of the channel number of the left detector, for electrons that give a coincidence with the Pb-glass on the right hand side. For the left detector, only channels 2 – 14 are used. Events in the center region have a significant higher A_{zz} compared to events at the edge. Lower: $\text{Rate} \cdot A_{zz}$

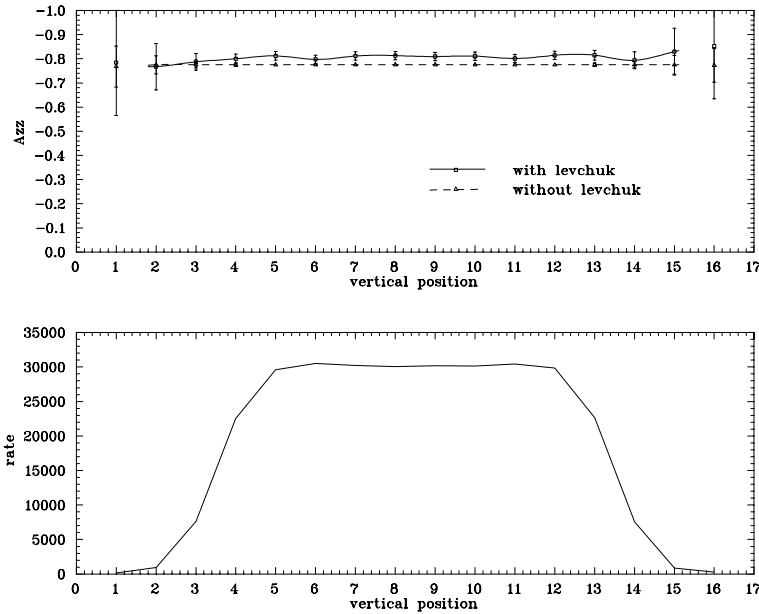


Figure 5.7: Monte Carlo simulation (vertical direction): Upper: A_{zz} as a function of the position orthogonally to the resolution of the hodoscope (vertically), for electrons that give a coincidence with the Pb-glass on the right hand side. For the left detector vertical position bins 2 – 14 are used. Lower: Rate

To calculate the analyzing power $\overline{A_{zz}}$ the following effects have been considered in the Monte Carlo program:

1. The magneto-optic design
2. The detector acceptances
3. Multiple scattering with Molliere tails
4. Radiative losses
5. The Levchuk effect

The analyzing power $\overline{A_{zz}}$ has been calculated for different energies and actual values are listed in Table 5.3.

Beam energy	$\overline{A_{zz}}$ without Levchuk	$\overline{A_{zz}}$ with Levchuk	correction
2 GeV	0.7744 ± 0.0001	0.7981 ± 0.0018	+ 3.06%
4 GeV	0.7755 ± 0.0002	0.7990 ± 0.0020	+ 3.03%
6 GeV	0.7758 ± 0.0002	0.7991 ± 0.0021	+ 3.00%

Table 5.3: Effective $\overline{A_{zz}}$ for different beam energies. The calculation includes Levchuk, multiple scattering, radiative tail and Bremsstrahlung effects. The target foil thickness used was 20 μm . For the uncertainty due to the knowledge of the atomic momentum distribution see Section A.

The first four effects are polarization independent and, standing alone, do not have an influence on $\overline{A_{zz}}$ ($\ll 0.1\%$). However in connection with the Levchuk effect a small influence of the multiple scattering can be seen ($\approx \pm 0.1\%$ for commonly used target-thicknesses), see Table 5.4.

$\overline{A_{zz}}$ correction relative to a 20 μm target (calculations include Levchuk effect)					
Beam energy	no MS	10 μm target	20 μm	40 μm	80 μm
2 GeV	+0.41%	+0.11%	0.0%	-0.17%	-0.21%
4 GeV	+0.52%	+0.14%	0.0%	-0.01%	-0.11%
6 GeV	+0.36%	+0.11%	0.0%	-0.05%	-0.06%

Table 5.4: $\overline{A_{zz}}$ dependence on the target thickness or the multiple scattering respectively.

Chapter 6

Outlook

A polarization measurement, reaching a final accuracy of below 1% will be more accurate than the errors required for most nuclear physics experiments. Therefore a further error reduction at the moment is not necessary.

There remains the goal of a completely non destructive polarization measurement, which can be performed in parallel with physics experiments. Any polarization change could then be observed immediately. Furthermore no experimental time at all would be used for the polarization measurement.

Non destructive polarization measurements can be done using compton backscattering. However this technique is, due to the very small rates, only applicable for high intensity machines with currents in the mA range. For the CEBAF hall C polarimeter we may reach this goal for currents in the μA range by the use of ultra thin iron targets.

Appendix A

Errors in the determination of beam polarization P_b

Symbols used:

P_b = Beam polarization

P_t = Target polarization

N^+, N^-, N = Number of Møller electrons detected with spins parallel, anti parallel and the total number of Møller pairs

$A_{zz} = -\frac{7}{9}$ Asymmetry coefficient for (90°) CM Møller scattering

$\overline{A_{zz}}$ = Average asymmetry for the detector acceptance.

The measured asymmetry A is:

$$A = \frac{N^+ - N^-}{N^+ + N^-} = \overline{A_{zz}} \cdot P_b \cdot P_t. \quad (\text{A.1})$$

Thus,

$$P_b = \frac{1}{\overline{A_{zz}} \cdot P_t} \cdot A, \quad (\text{A.2})$$

and hence,

$$\frac{\Delta P_b}{P_b} = \sqrt{\left(\frac{\Delta A}{A}\right)_{stat.}^2 + \left(\frac{\Delta \overline{A_{zz}}}{\overline{A_{zz}}}\right)_{syst.}^2 + \left(\frac{\Delta P_t}{P_t}\right)_{stat.+syst.}^2}. \quad (\text{A.3})$$

As shown in the preceding formula, there are three error contributions occurring in the calculations of the beam polarization, the first one being statistical, the second one being systematic in nature and the third one a combination of both. We discuss the systematic uncertainties first.

A.1 Systematic error in $\overline{A_{zz}}$

There are two main contributions which lead to an error in $\overline{A_{zz}}$.

- Accuracy of the Levchuk correction
- Geometrical alignment and beam optics

A.1.1 Accuracy of the Levchuk correction

As mentioned in Chapter 5.3 the intra atomic motion of bound electrons requires a correction for the asymmetry coefficient A_{zz} . The correction depends on the knowledge of the electron momentum distribution, the actual geometry and optics setup. We are calculating this correction with the aid of a Monte Carlo program [Sw95].

The uncertainty, based on the calculated atomic momentum distribution was estimated by comparing results using real distributions [Sw95] with results using delta function distributions [Le94]. For the SLAC single arm Møller polarimeter Swartz found a Levchuk effect of 14% and a difference due to the distributions of $\pm 0.2\%$. For the CEBAF polarimeter we found a correction in the order of 3% where the error due to the atomic momentum distribution is not detectable within our statistic error of $\pm 0.2\%$. A complete list for different beam energies is given in Table A.1.

Beam energy	$\overline{A_{zz}}$ without Levchuk effect	$\overline{A_{zz}}$ with Levchuk effect	correction
2 GeV	0.7744 ± 0.0001	0.7981 ± 0.0018	+ 3.06%
4 GeV	0.7755 ± 0.0002	0.7990 ± 0.0020	+ 3.03%
6 GeV	0.7758 ± 0.0002	0.7991 ± 0.0021	+ 3.00%

Table A.1: Effective $\overline{A_{zz}}$ for different beam energies. The calculation includes Levchuk, multiple scattering, radiative tail and Bremsstrahlung effects. Target foil thicknesses of 10 – 40 μm did within the errors not change these results.

A.1.2 Geometrical alignment and beam optics

The *systematic* contribution $\Delta\overline{A_{zz}}$ can be determined in the following way:

$$\overline{A_{zz}}(\theta_{a,b}) = \frac{\int_{\theta_a}^{\theta_b} A_{zz}(\theta) \cdot \sigma(\theta) d(\theta)}{\int \sigma(\theta) d(\theta)}, \quad (\text{A.4})$$

where we integrate over the θ acceptance of the shower counter (eg. 83° to 97° CM angle). By integrating over angular ranges corresponding to a detector center displaced from 90°

CM angle, we get the deviation in $\overline{A_{zz}}$ corresponding to a horizontal misalignment of the detector. Fig. A.1 shows $\overline{A_{zz}}$ as a function of detector center position (upper graph) and the relative error as a function of detector position.

A priori there is no dependence off $\overline{A_{zz}}$ on the ϕ (vertical) acceptance or position of the detectors. However if we start to loose events due to a large vertical misalignment the sensitivity to polarization dependent beam shifts increases strongly.

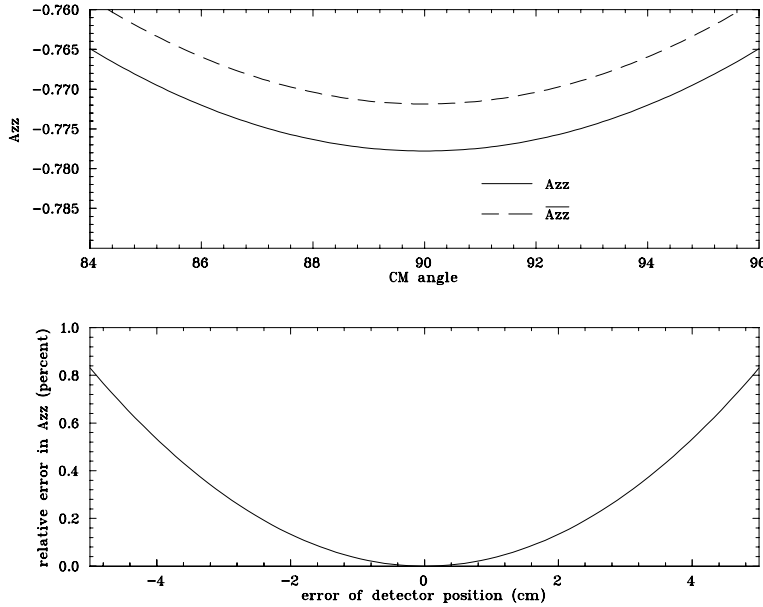


Figure A.1: Error in $\overline{A_{zz}}$ as a function of the horizontal detector misalignment. Upper graph: A_{zz} for point-like acceptance (solid) and $\overline{A_{zz}}$ for a detector acceptance $\theta = \pm 7^\circ$ CM (dashed). Lower graph: Relative error of $\overline{A_{zz}}$ as a function of the horizontal misalignment of the detectors.

Examples of horizontal misalignment ¹ and the effects on $\overline{A_{zz}}$ are shown in Table A.2:

Error due to	amount	change of $\overline{A_{zz}}$
beam position	1.0 mm	0.03%
beam angle	0.2 mrad	0.04%
detector positions	2.0 mm	< 0.01%
total uncertainty		0.05%

Table A.2: Errors due to misalignment or mistuning.

A horizontal displacement of one of the quadrupoles from the beam line center has, to first order, the same error effect as a displaced beam. This is due to the fact that the quadrupole makes the main separation between the Møller electrons and the beam.

An accuracy of better than a millimeter leads to a relative systematic error in $\overline{A_{zz}}$, as shown in Figure A.1.

¹Vertical misalignments (position and angle) do lead to a coincidence loss only.

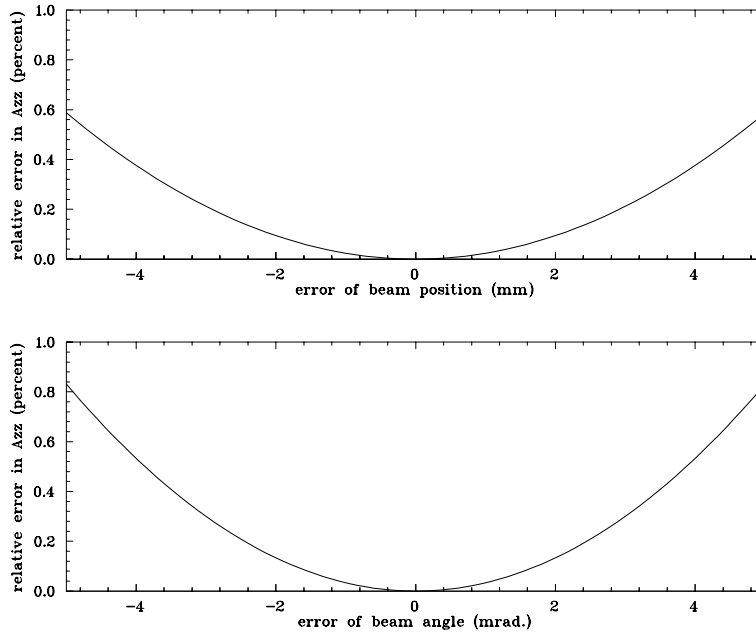


Figure A.2: Error in $\overline{A_{zz}}$ as a function of horizontal beam misalignment.

Working with standard survey accuracies ($< 100\mu m$) the geometry has no influence on the $\overline{A_{zz}}$ accuracy. For a correct alignment, any shifts of the beam cancel out to first order.

A.2 Error in target polarization P_t

The Kerr measurement of the foil magnetization reaches a relative accuracy of 0.25%. This however is possible up to 250⁰ foil temperature only (see chapter 4, Figure 4.9).

The systematic error due to geometrical misalignment or a warping of the target foil has been estimated to be smaller than 0.25% (see chapter 3.2.2, Figure 3.5).

The absolute magnetization of iron is known to an accuracy of 0.1% [Gr82], the resulting electron polarization to 0.18% (Chapter 3, Table 3.1).

The final error introduced by the target polarization is shown in Table A.3.

Error due to:	estimated error
Kerr measurement (statistics)	$<0.25\%$
target foil orientation	$<0.25\%$
absolute magnetization (systematics)	0.18%
total uncertainty	$<0.4\%$

Table A.3: Error of the target polarization

A.3 Statistical errors and count rate estimates

To estimate the measuring time, we assume a typical low current, high polarization experiment:

$$P_b = 0.8$$

$$P_t = 0.08043 \text{ [Table 3.1]}$$

A = Measured asymmetry (see, Equation A.1)

From equation (A.1), we note that for $N^- \simeq N^+$,

$$\Delta A \simeq \sqrt{\frac{1}{N}} . \quad (\text{A.5})$$

We use equation's (A.2) and (A.3) to obtain

$$\frac{\Delta P_b}{P_b} \simeq \frac{\Delta A}{A} = \frac{1}{0.0529 \cdot \sqrt{N}} , \quad (\text{A.6})$$

where we have ignored the systematical errors for the moment. Therefore, in order to obtain $\frac{\Delta P_b}{P_b} \leq 1\%$ we need to detect $\geq 3.6 \cdot 10^6$ Møller pairs.

Because it is not trivial to transform the detector shape (which was designed with the image of the scattered Møller electrons corresponding to the CM frame) into the lab frame, I made all acceptance estimations using the CM acceptance of the detectors. The CM acceptance will be 46 msr at 4 GeV for detectors described in chapter 2. To a first approximation, the Møller cross section is constant over the whole detector acceptance, which is symmetric about 90° CM angle.

The rate per second R is:

$$R = d \cdot N_a \cdot \frac{Z}{A} \cdot N_b \frac{d\sigma}{d\Omega_{CM}} \cdot \Delta\Omega_{CM} . \quad (\text{A.7})$$

$$d = \text{target thickness} = 0.0158 \left[\frac{g}{cm^2} \right] \text{ (20 } \mu\text{m Fe foil)}$$

$$N_a = \text{Avogadros number} = 6.02 \cdot 10^{23}$$

$$\frac{Z}{A} = 0.466 \text{ (pure iron)}$$

$$N_b = 6.25 \cdot 10^{12} \left[\frac{e^-}{second} \right] \text{ (assuming } 1\mu\text{ A)}$$

$$\Delta\Omega_{CM}(4GeV) = 46 \cdot 10^{-3} [sr]$$

$$\frac{d\sigma}{d\Omega_{CM}(4GeV)} = 4.56 \cdot 10^{-5} \left[\frac{barn}{sr} \right] = 4.56 \left[\frac{fm^2}{msr} \right]$$

For count rates and measuring times with a $20\mu\text{m}$ Fe foil at 4 GeV incident electron energy we get the following values (note that we have assumed perfect detector efficiency and no coincidence losses), Table A.4:

Beam current in μA	Count rate in kHz	Measuring time for $\frac{\Delta P}{P}=1\%$
0.1	5.8	620 sec
1	58	62 sec
10	580	6.2 sec

Table A.4: Count rate and measuring time for $\frac{\Delta P}{P}=1\%$ and 4 GeV beam energy.

The detector acceptance changes with the incident electron energy. The measuring times for $\frac{\Delta P}{P}=1\%$ therefore change as well. In Table A.5 values for different beam energies at $1\mu\text{A}$ current are listed.

E-beam (GeV)	Cross section $\frac{d\sigma}{d\Omega_{CM}}(\frac{fm^2}{msr})$	CM-Acceptance (msr)	Time for $\frac{\Delta P}{P}=1\%$
1	18.2	65	10 sec
2	9.1	57	25 sec
3	6.1	49	43 sec
4	4.5	46	62 sec
5	3.6	44	81 sec
6	3.0	43	100 sec

Table A.5: Cross section and measuring time for different beam energies.

Appendix B

Tuning procedure for the Møller Polarimeter

This chapter describes a procedure for finding the optimal initial tuning of the polarimeter. Before starting with the tuning procedure I strongly recommend to have a close look to chapter 2 especially the following Figures:

- The general setup of the quadrupoles and detectors, shown in Figure 2.3.
- The desired Møller event distributions in the detector plane, shown in Figure 2.4.

Apart from the timing, there are three things we need to tune properly: The small quadrupole, the large quadrupole and the incident beam position. A priori it is not possible to disentangle all three completely, especially the two quadrupoles! With the aid of the hodoscope we will be able to optimize the whole setup within a few steps.

B.1 Timing

For a better understanding I recommend to consider the electronics diagram (Figure 2.9) and the detector arrangement (Figure 2.8) first.

The adjustment of the timing is possible by the use of the pulser system. Light pulses of about 5 ns width (adjustable in width and amplitude) are generated by a fast laser diode. The light pulses are distributed by a 44 channel splitter cable. The hodoscope detectors and the lead glass detectors do get light pulses at exactly the same time.

With these pulses we can adjust the timing of all detectors relative to each other. Nevertheless a cross check with real events should be made after the magneto-optic tuning is completed (described in the next section).

B.2 Magnet and beam optics

1. Set the two quadrupoles to their calculated values and accumulate some data in the hodoscope.
2. Vary the current of the large quadrupole such, that the distribution which might be like in Figure B.2 gets centered like in Figure B.1. For rough adjustments: maximize the lead glass coincidence rate.

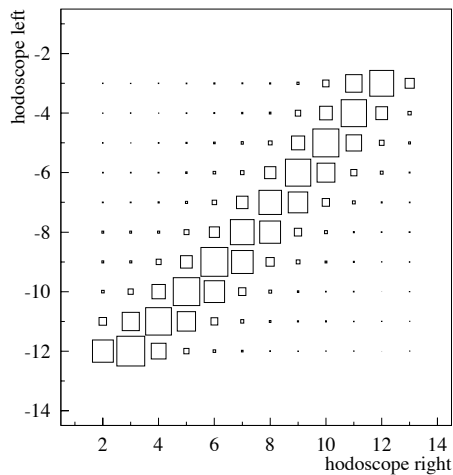


Figure B.1: Event pattern hodoscope left versus hodoscope right. Perfect tuning of the small and the large quadrupole. Hodoscope events are distributed symmetrically with a very slight curvature along the diagonal line of the graph.

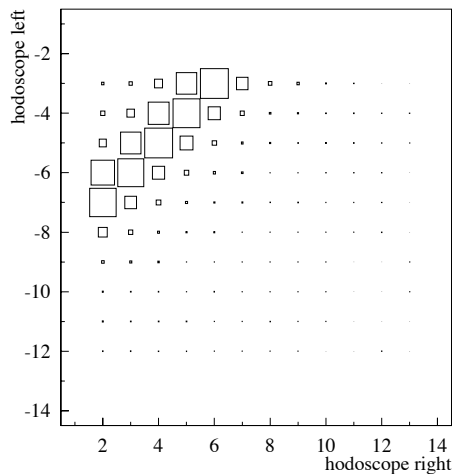


Figure B.2: Event pattern hodoscope left versus hodoscope right. A too small value of the large quadrupole is seen in a shift of the ridge formed by the hodoscope events, towards the upper left edge of the graph for a too high quadrupole setting.

3. The distribution might be relatively wide like in Figure B.3. Vary the current of the small quadrupole and try to get it as narrow as possible. This works only for small changes, for large changes one needs to reoptimize the large quad (2.) and try with the small quad again. Repeat this until the best possible solution is found. Watch the coincidence rate! If it gets smaller even after reoptimizing the large quad (2.) you have chosen a too large value for the small quad.

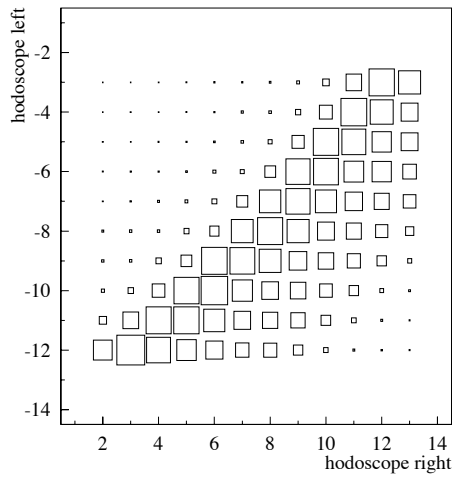


Figure B.3: Event pattern hodoscope left versus hodoscope right. A too small value of the small quadrupole is seen in a broadening of the ridge formed by the hodoscope events.

4. Now we need to check the beam tuning. The up/down tuning can be checked with the count rate in the splitted hodoscope channels or the final lead glass coincidence rate. The countrates of upper and lower channels as a function of the beam position are shown in Figure B.4.

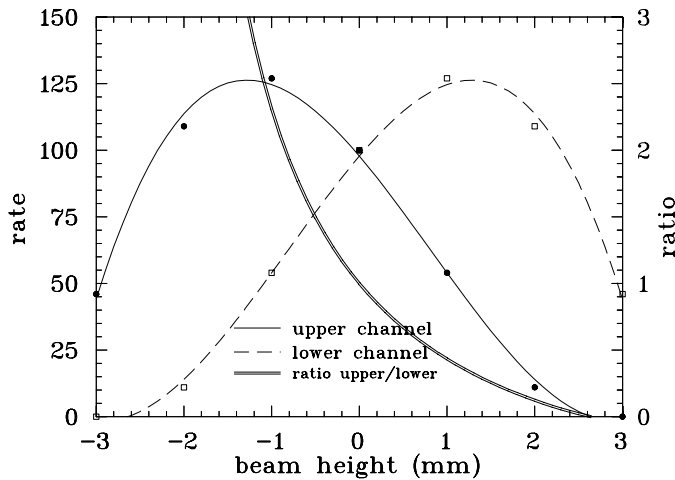


Figure B.4: Rate of events in the splitted hodoscope channels. Upper channel (solid), lower channel (dashed). Right-hand scale: ratio upper/lower

5. The left/right tuning is more difficult to check as the system is less sensitive to that. Nevertheless, if the distribution has a small asymmetric curvature like in Figure B.5 the beam is off center to the left (to see the difference, compare with the optimal tuning shown in Figure B.1).

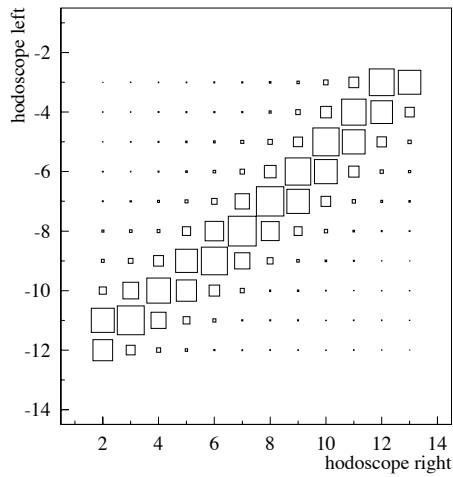


Figure B.5: Perfect tuning of the quadrupoles but beam 5 mm off center (to the left). The lower end of the ridge formed by the hodoscope events is curved about 1 channel to the left.

To get a better idea of what actually happens with the events, the detector arrangement is shown in Chapter 2, Figure 2.8. The effect of different beam mistunings are shown in the Figures below.

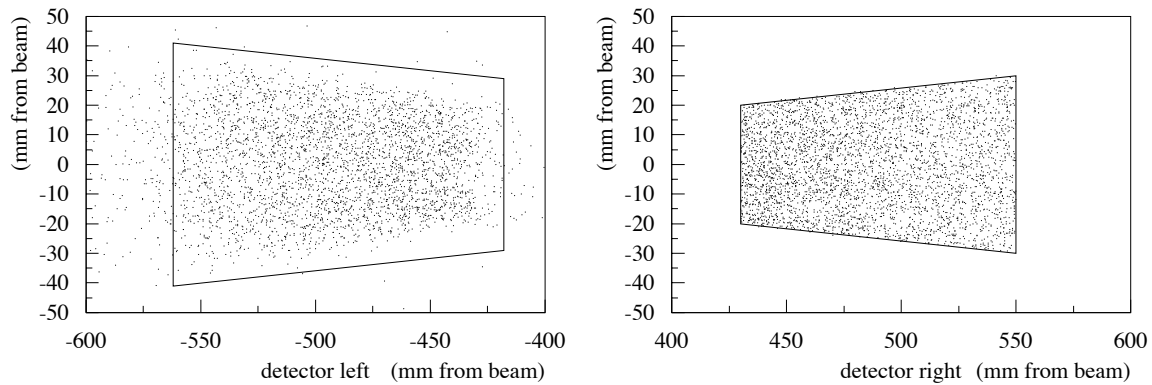


Figure B.6: Møller event distribution in the detector plane, for a correctly tuned beam. The left detector has a larger acceptance which results in less sensitivity to any mistunings.

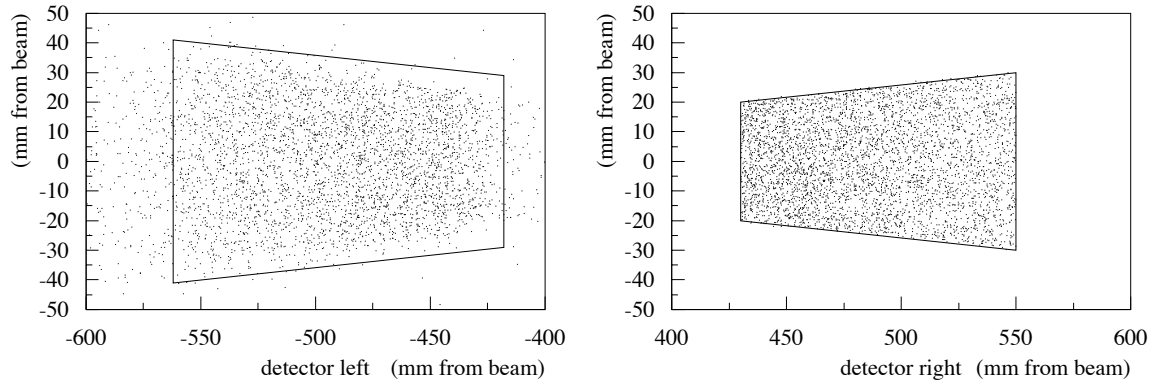


Figure B.7: Møller event distribution in the detector plane, for a beam 5 mm to the left of the nominal axis. Events in the left detector are shifted to the left and broadened.

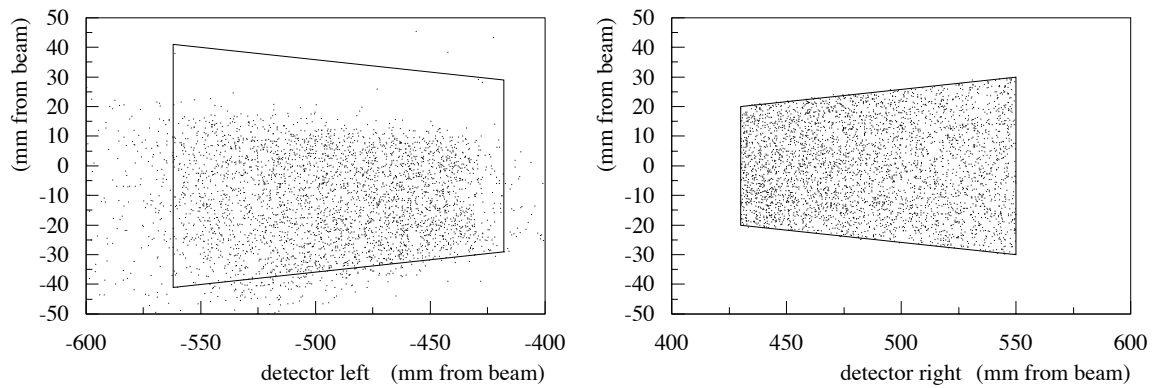


Figure B.8: Møller event distribution in the detector plane, for a beam which is 1 mm too high. Events in the left detector are shifted down.

B.3 Quadrupole settings

The current settings of the two quadrupoles have been calculated for the optimal coincidence rate and the optimal hodoscope resolution. They should be used to start with and optimized like described in section B.2.

E_{beam} [MeV]	Q1 $\frac{dB}{dx} \cdot l_{eff}$ [T]	Q1 current [A]	Q2 $\frac{dB}{dx} \cdot l_{eff}$ [T]	Q2 current [A]
1000	1.141	69.6	1.206	136.9
1500	1.418	88.8	1.929	207.2
2000	1.603	102.2	2.721	288.3
2500	1.724	111.1	3.577	380.7
3000	1.798	116.7	4.497	485.3
3500	1.839	119.9	5.476	603.0
4000	1.856	121.1	6.513	734.5
4500	1.853	121.0	7.606	880.9
5000	1.838	119.8	8.753	1043.1
5500	1.798	116.8	9.955	1222.6
6000	1.779	115.3	11.201	1418.7

Table B.1: Calculated quadrupole current settings. Currents have been calculated using measured I versus B calibrations and include slight saturation effects at high fields. The effective field lengths used are 35.24cm cm and 99.06 cm respectively.

Appendix C

CADs

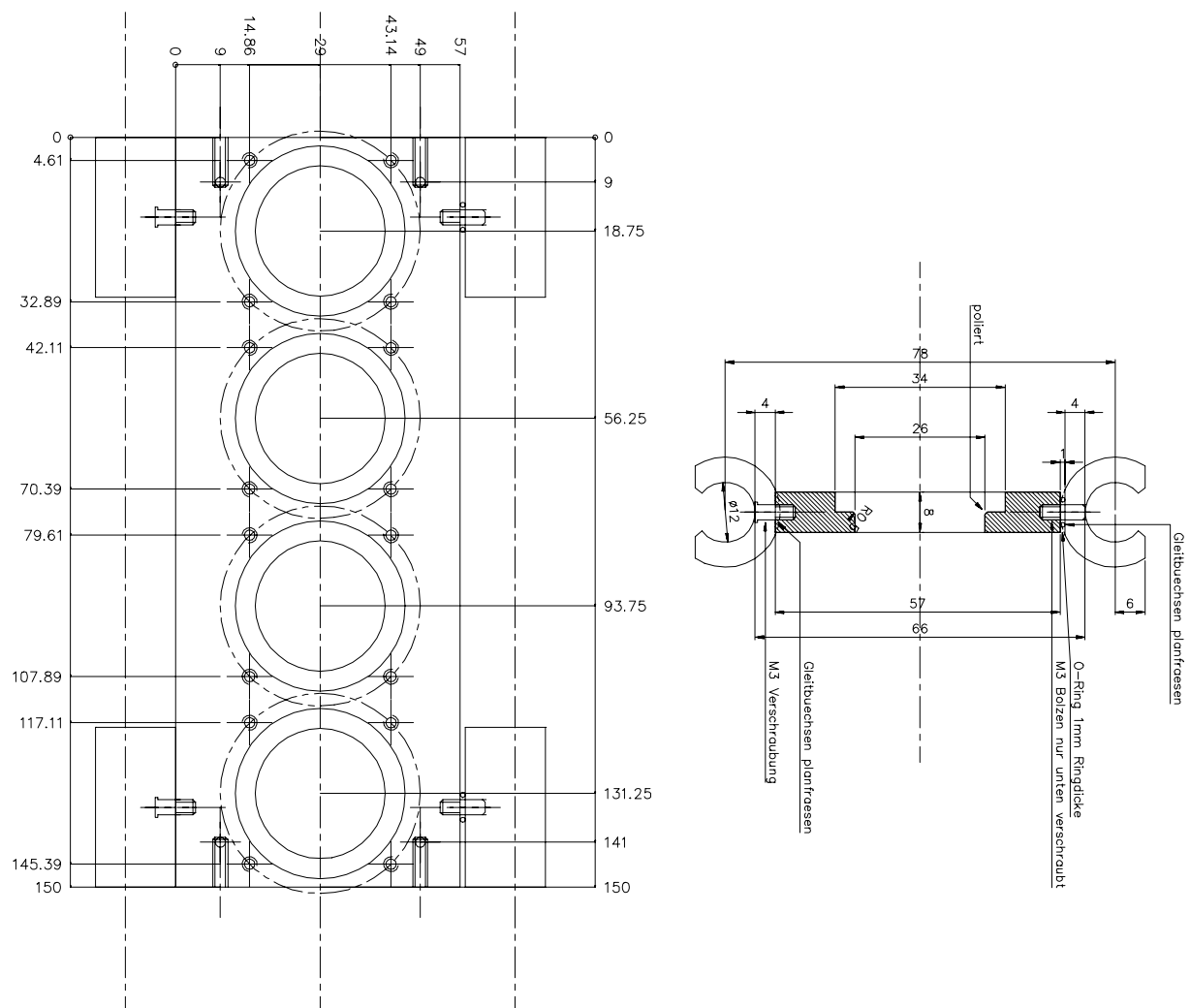


Figure C.1: Target: side view

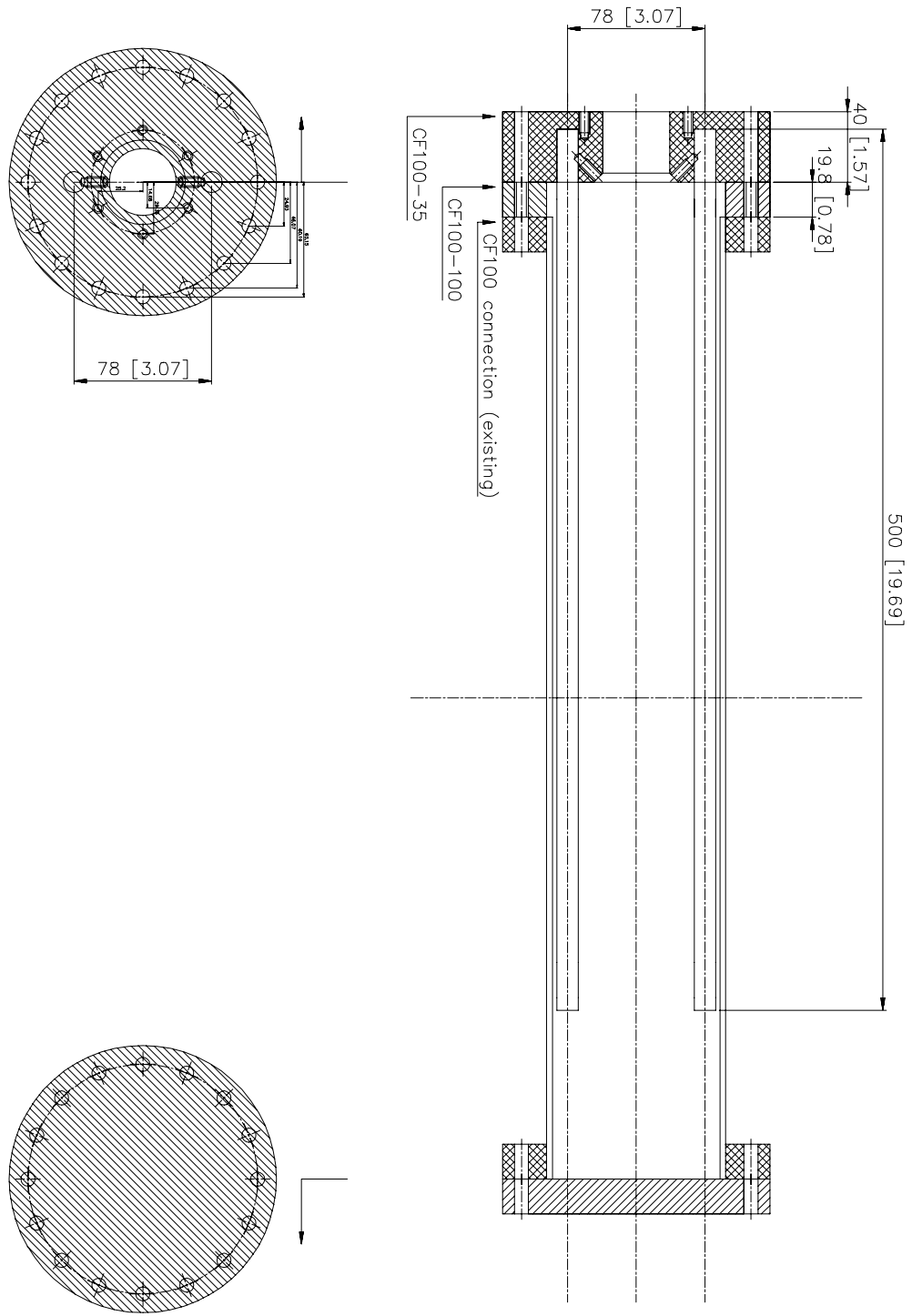


Figure C.2: Target rail system

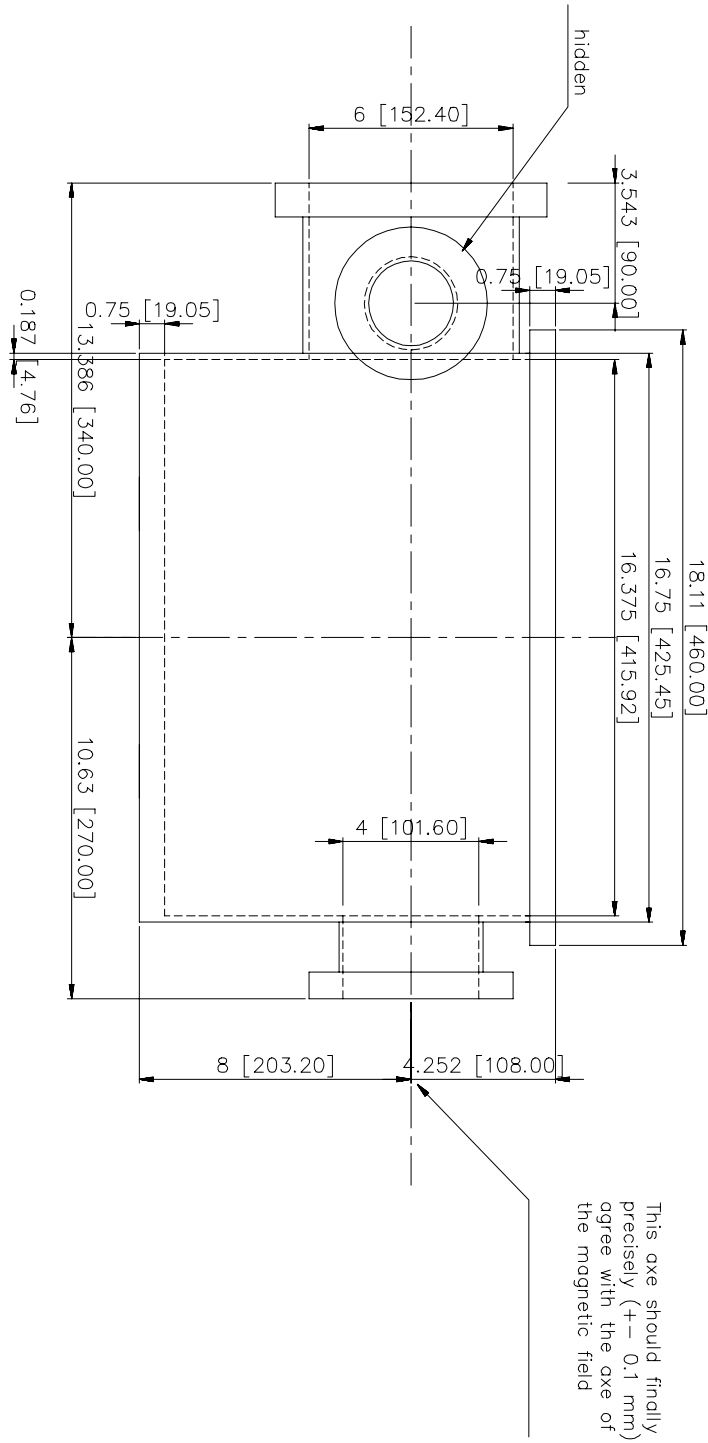


Figure C.3: Target chamber: side view

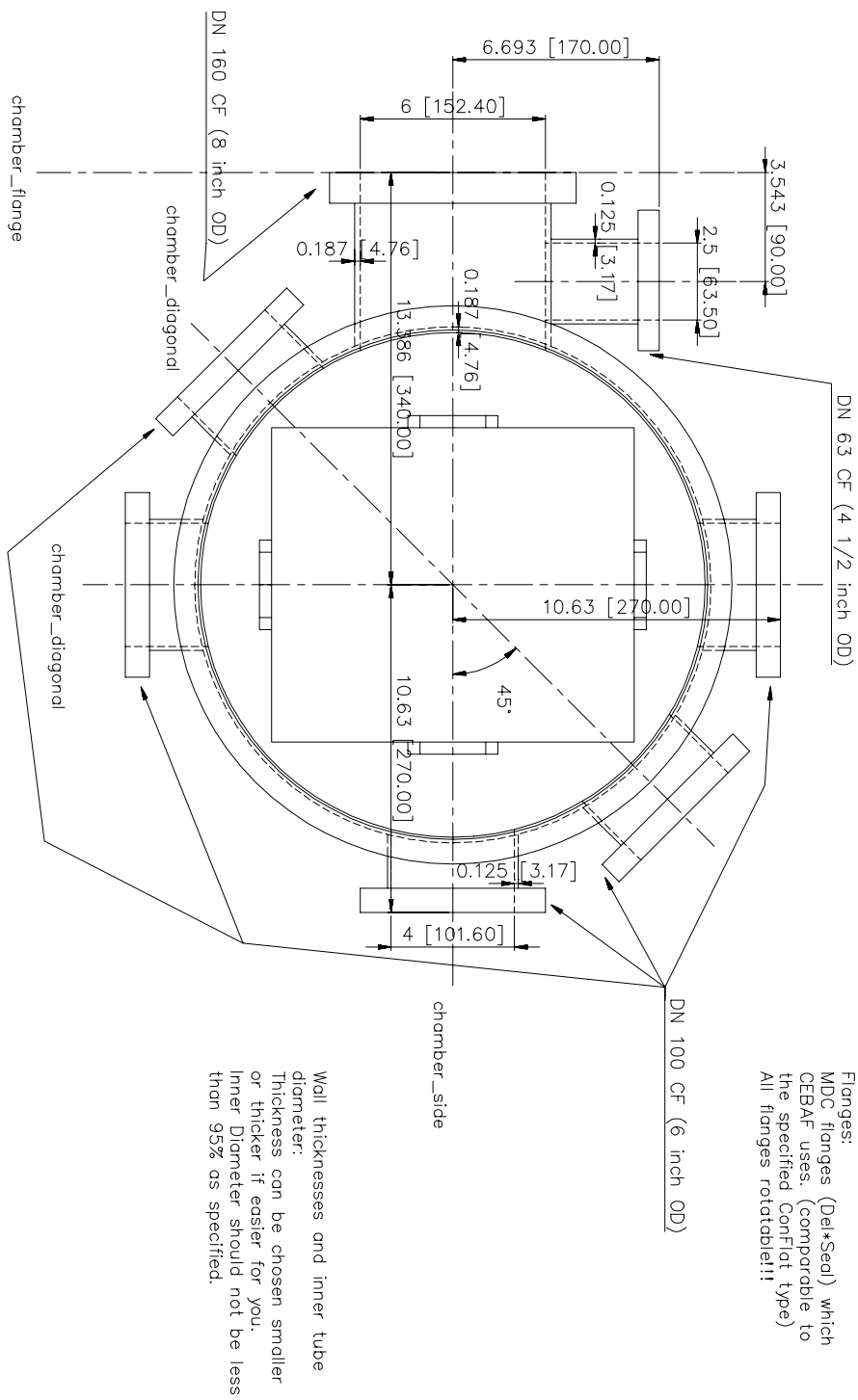


Figure C.4: Target chamber: top view

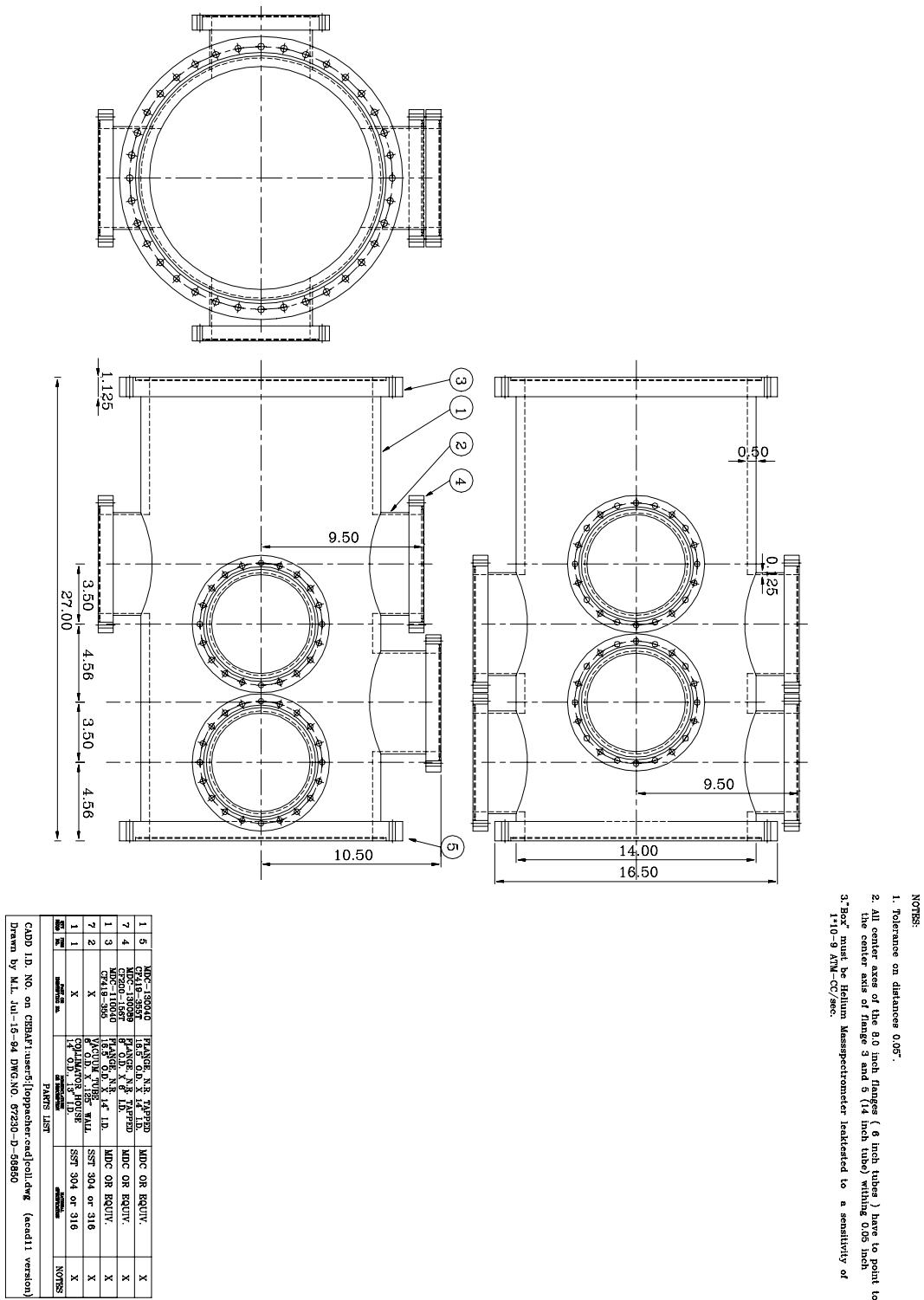


Figure C.5: Collimator vacuum can

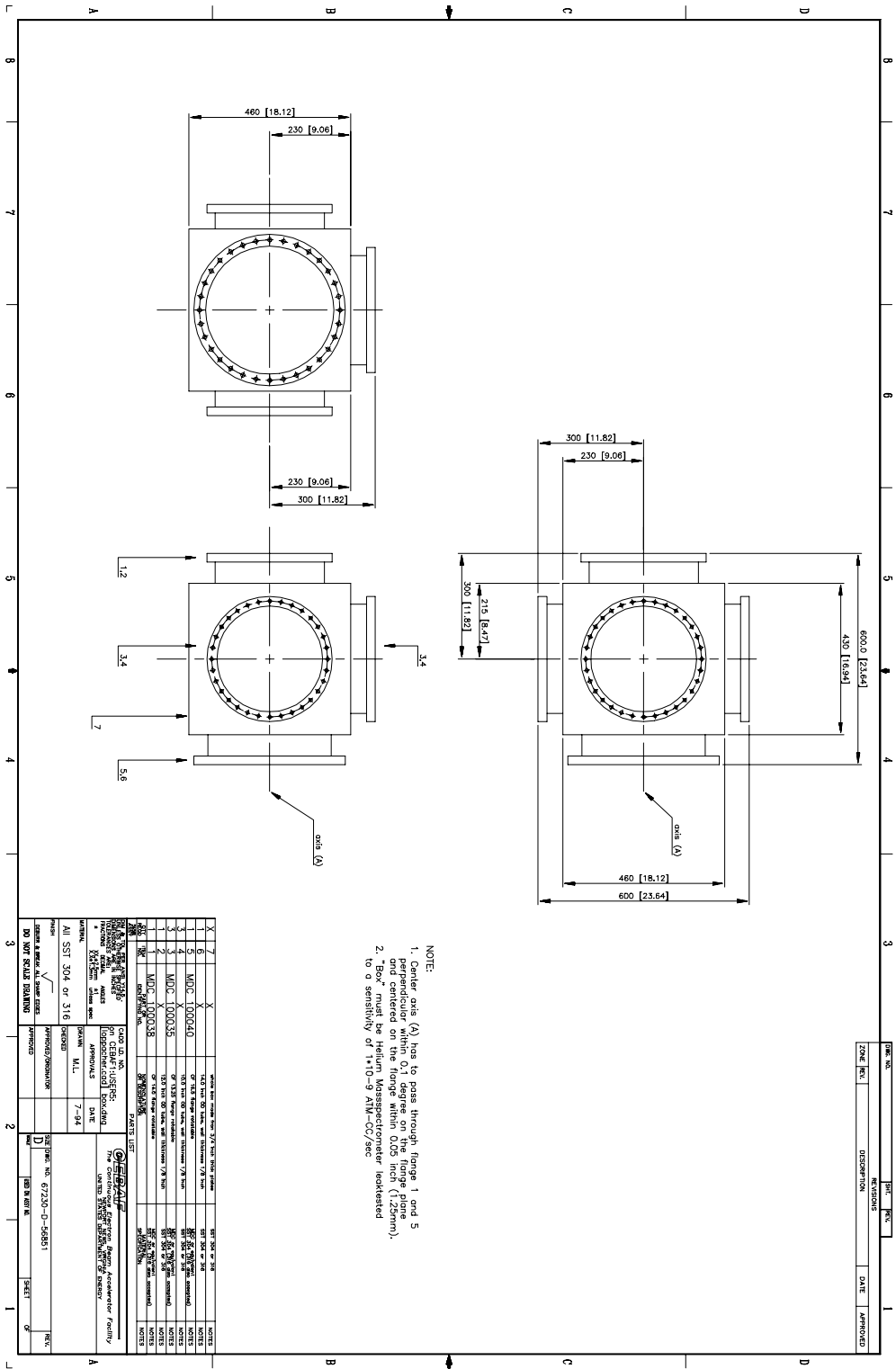


Figure C.6: Small vacuum can

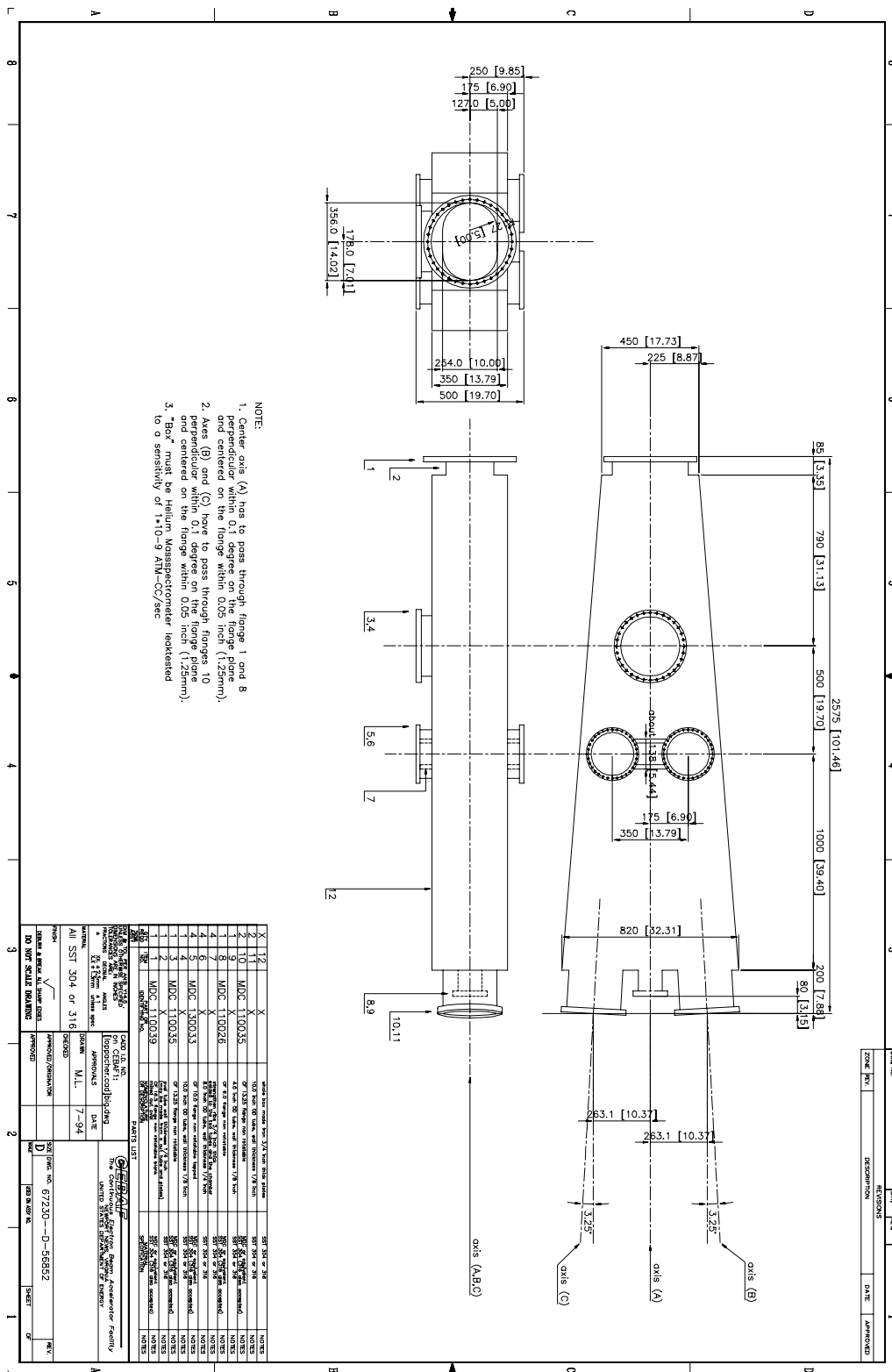


Figure C.7: Y-vacuum can

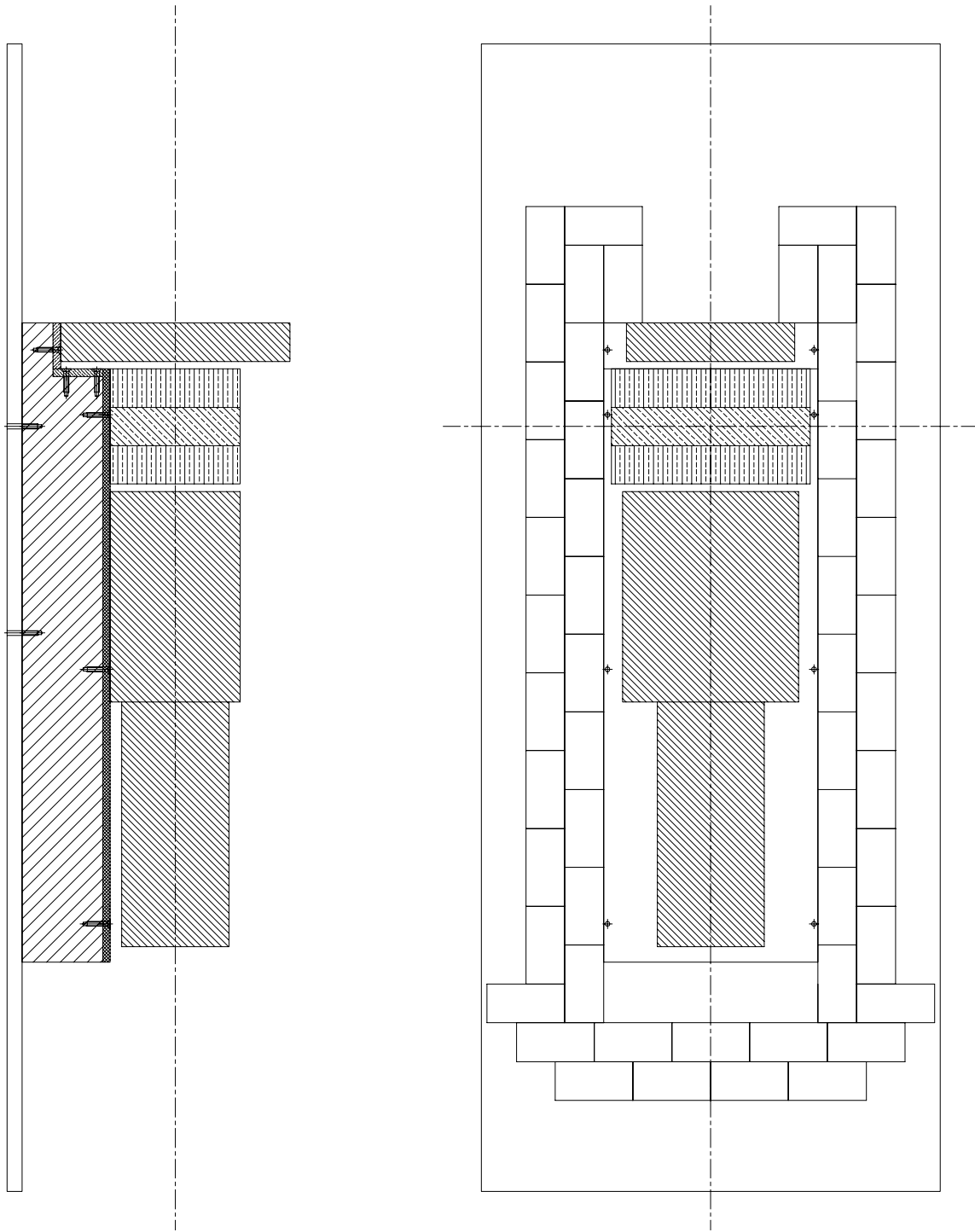
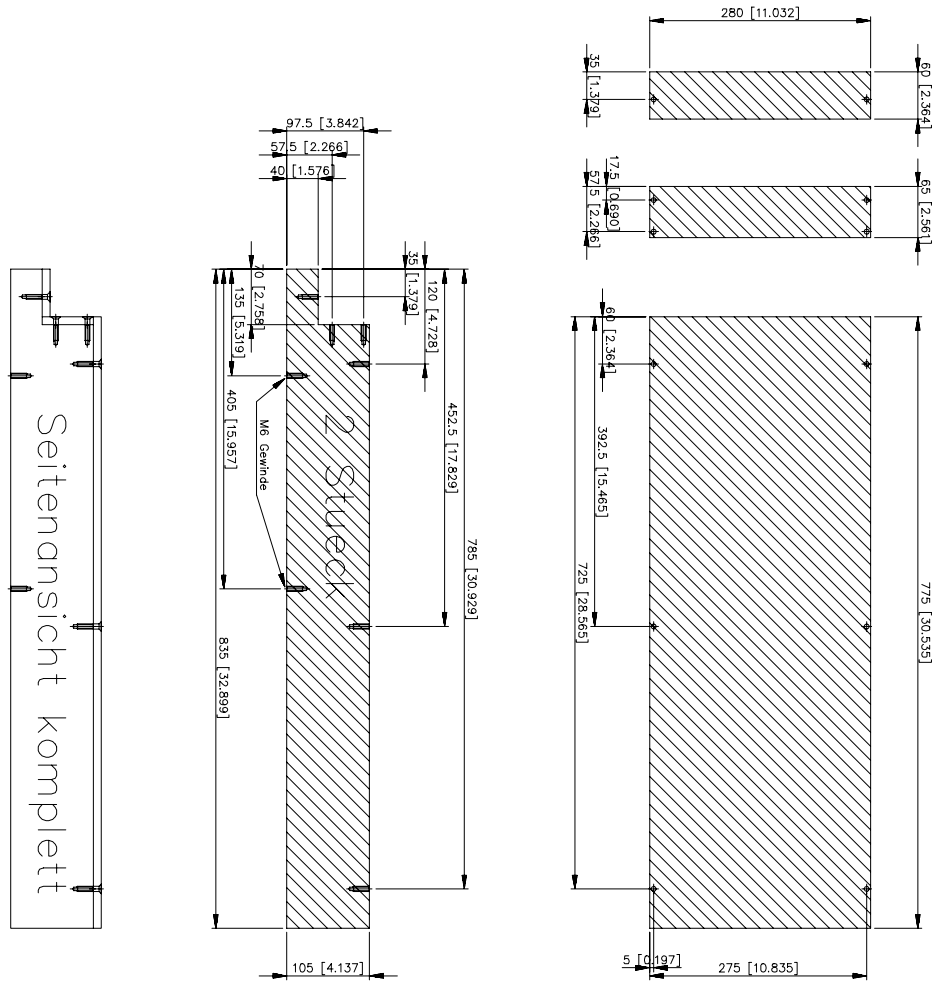


Figure C.8: Arrangement on the detector platform



Ministand:
 Material: 10mm Aluminium
 Bohrungen: M5
 Gewinde: M5, 10mm tief
 Anzahl: je ein Stueck ausser
 wo anders vermerkt
 Toleranzen: Teile muessen
 zusammenpassen

Figure C.9: Table top for detectors

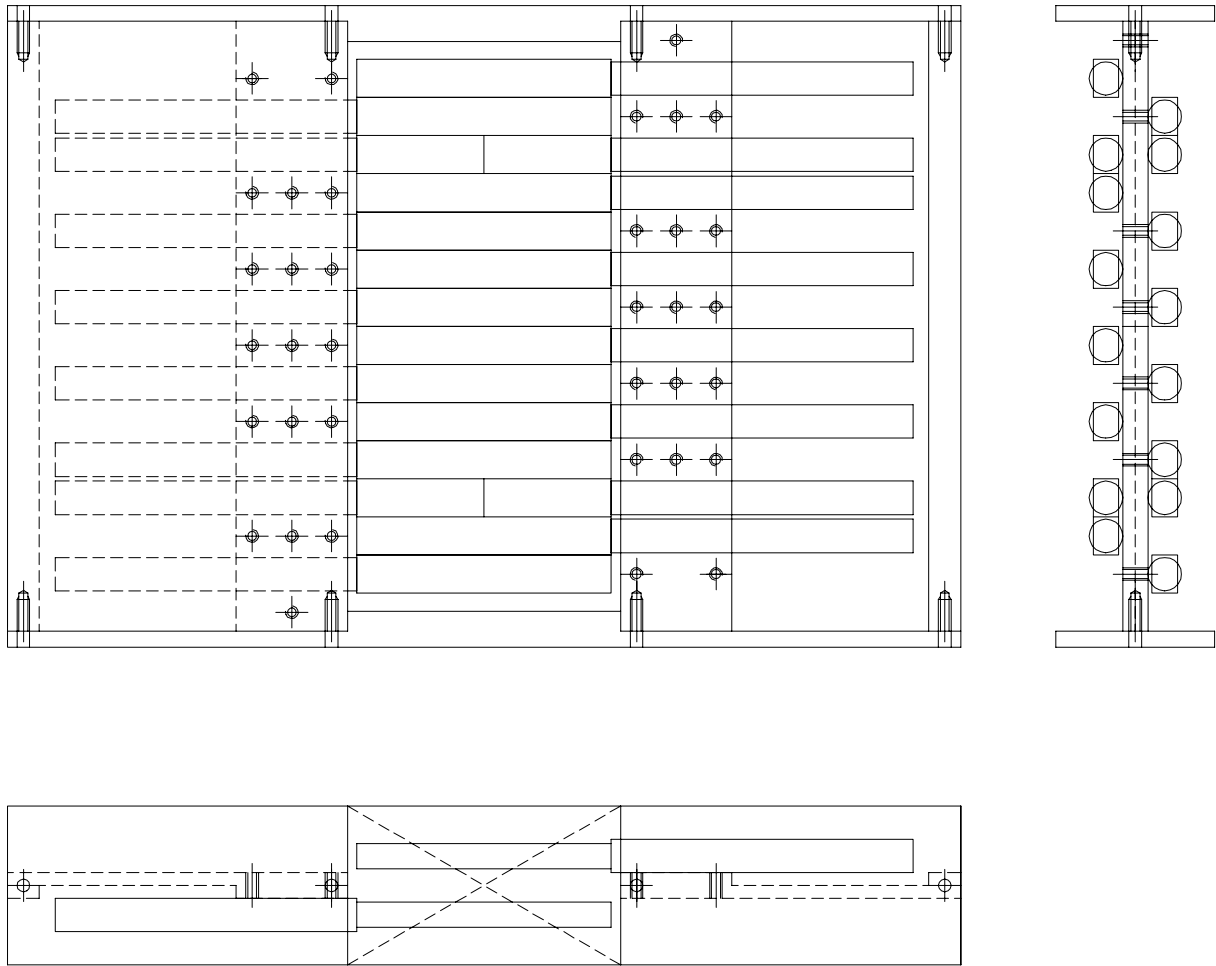


Figure C.10: Hodoscope mounting frame

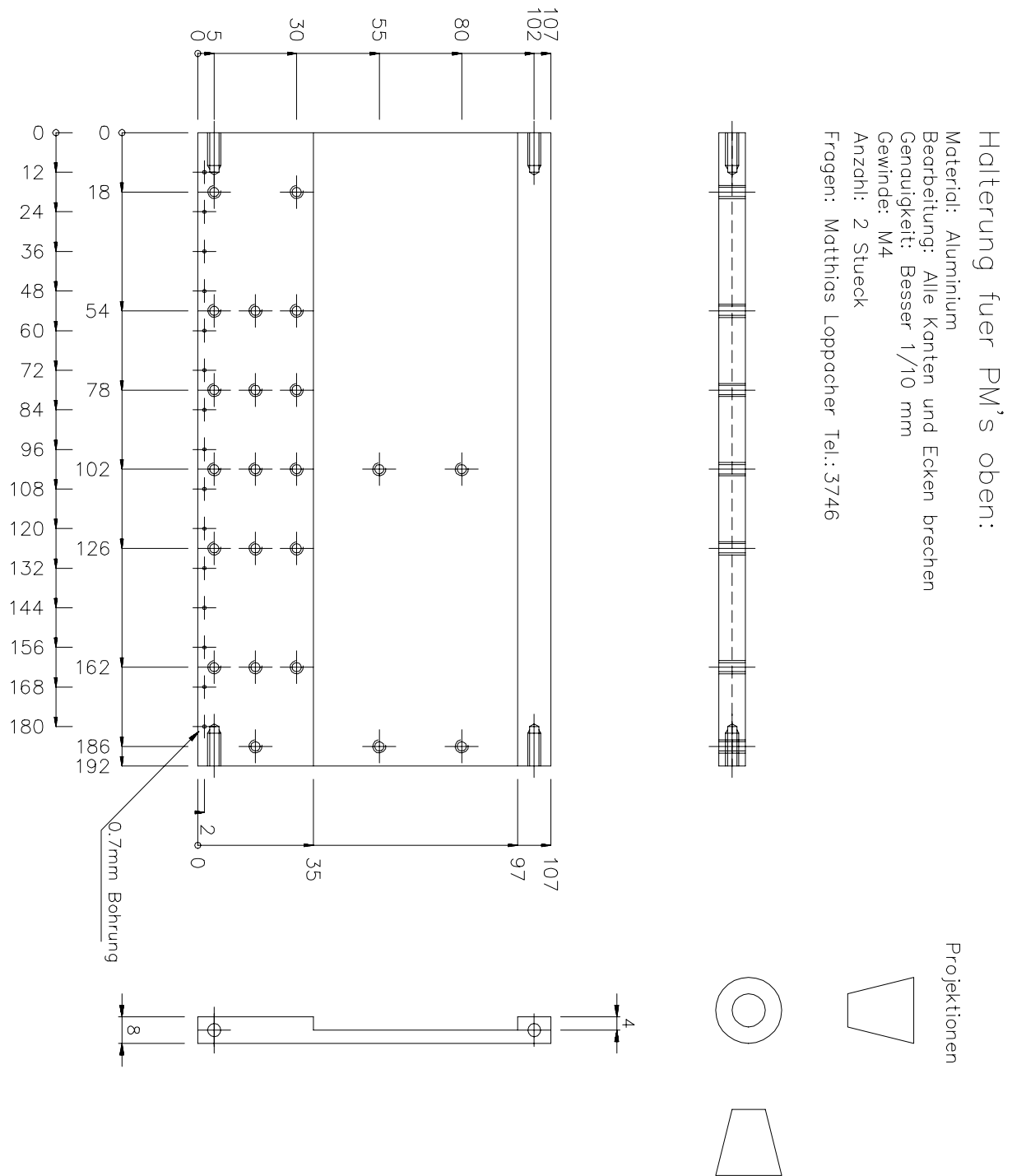
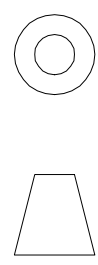
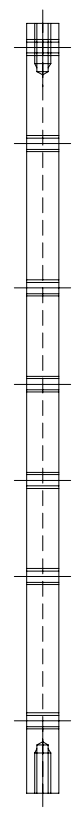


Figure C.11: Hodoscope PM plane 1

Halterung fuer PM's unten:

Material: Aluminium
 Bearbeitung: Alle Kanten und Ecken brechen
 Genauigkeit: Besser 1/10 mm
 Gewinde: M4
 Anzahl: 2 Stueck
 Fragen: Matthias Loppacher Tel.: 3746



Projektionen

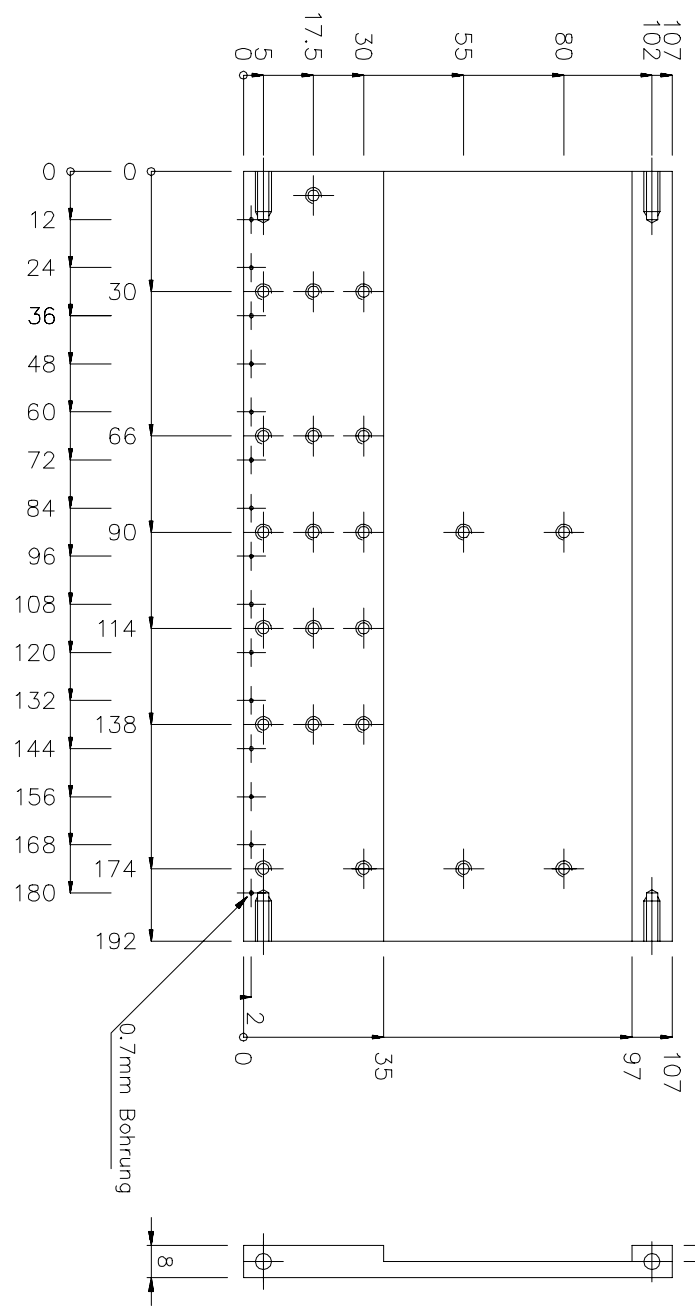


Figure C.12: Hodoscope PM plane 2

Verbindungsstücke:

Material: Aluminium
 Bearbeitung: Alle Kanten und Ecken brechen
 Genauigkeit: Besser 1/10 mm
 Bohrungen: passend zu M4 Schraube
 Anzahl: 2 Stueck
 Fragen: Matthias Loppacher Tel.: 3746

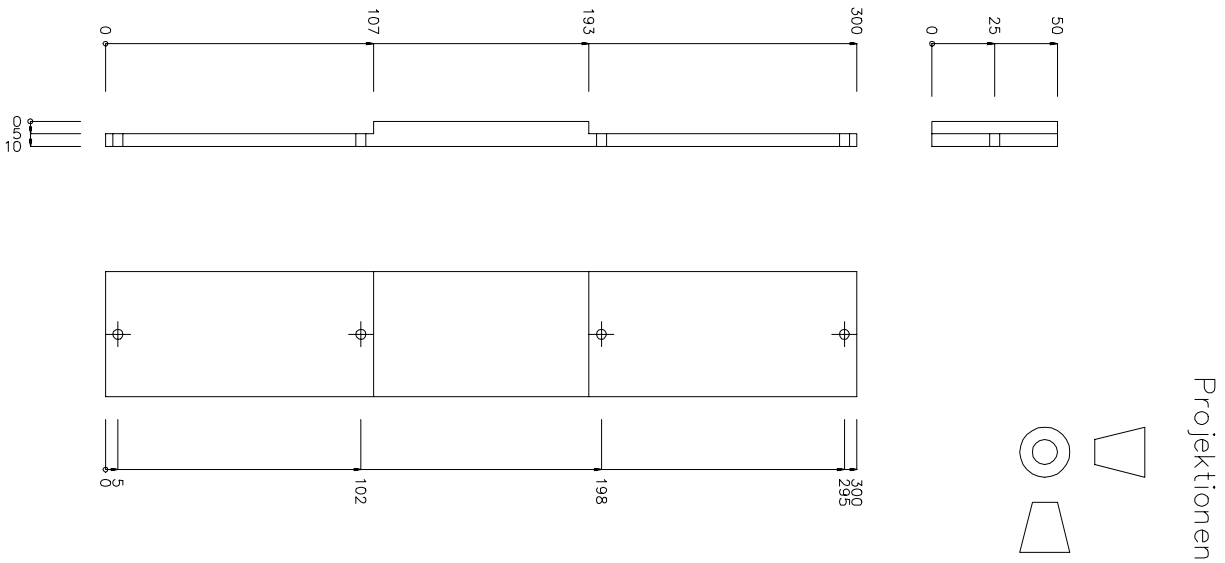


Figure C.13: Hodoscope side plane 1

Verbindungsstücke:

Material: Aluminium
 Bearbeitung: Alle Kanten und Ecken brechen
 Genauigkeit: Besser 1/10 mm
 Bohrungen: passend zu M4 Schraube
 Anzahl: 2 Stück
 Fragen: Matthias Loppacher Tel.: 3746

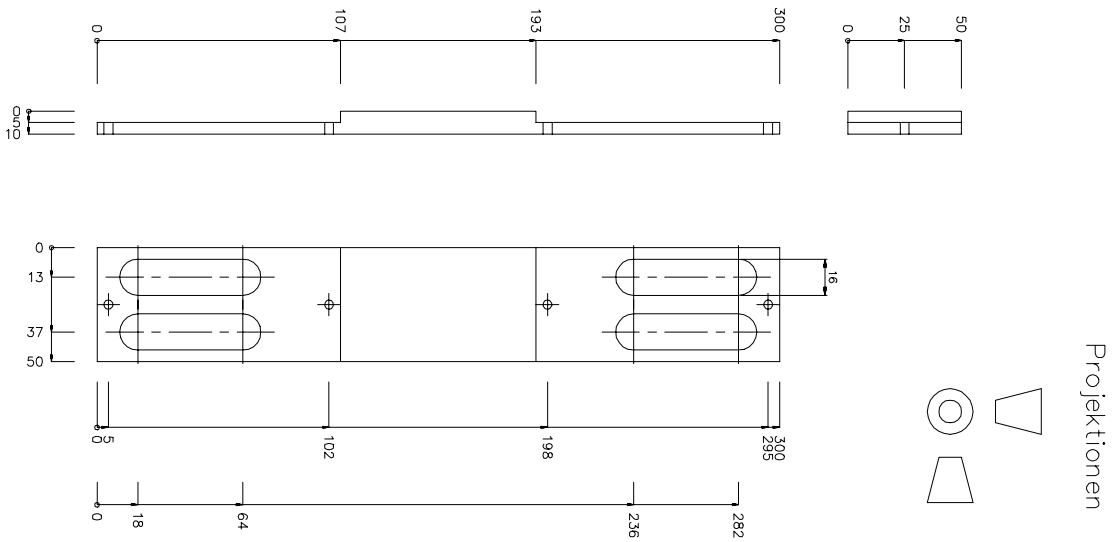


Figure C.14: Hodoscope side plane 2

Klemmen fuer PM's

Material: Aluminium

Bearbeitung: Alle Kanten und Ecken brechen

Genauigkeit: Besser 1/10 mm

Bohrungen: 4.5mm

Anzahl: 8 resp. 16 Stueck

Fragen: Matthias Loppacher Tel. 3746

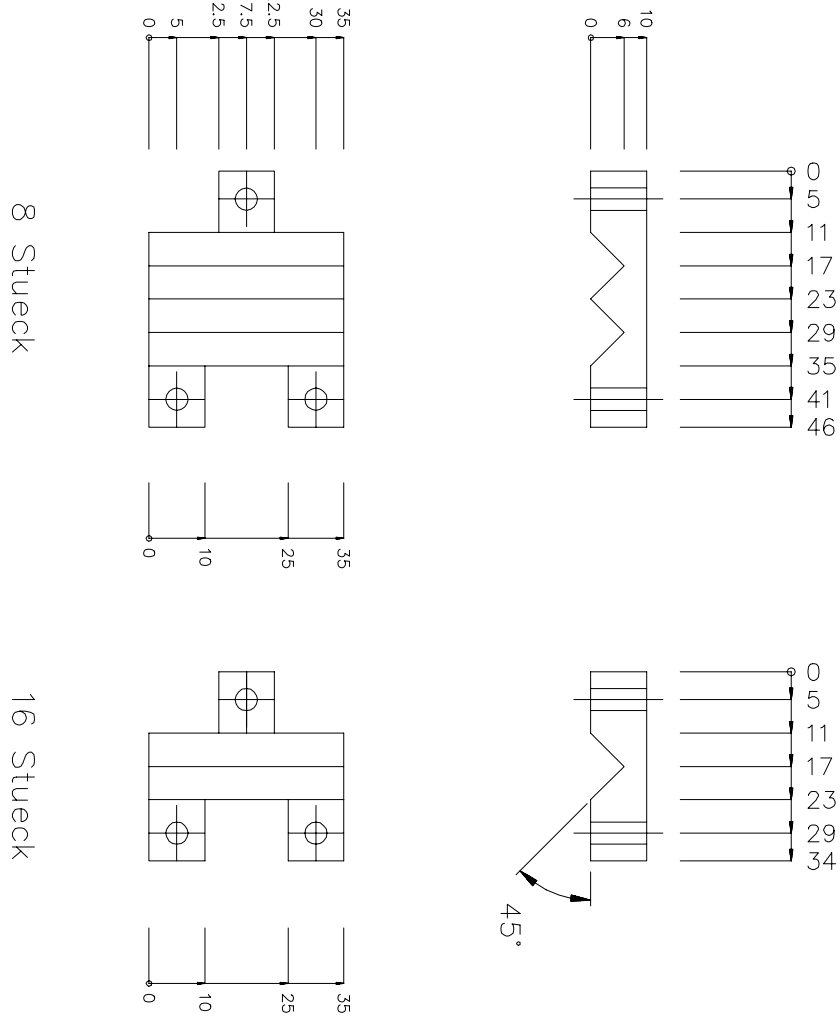


Figure C.15: Hodoscope PM clamps

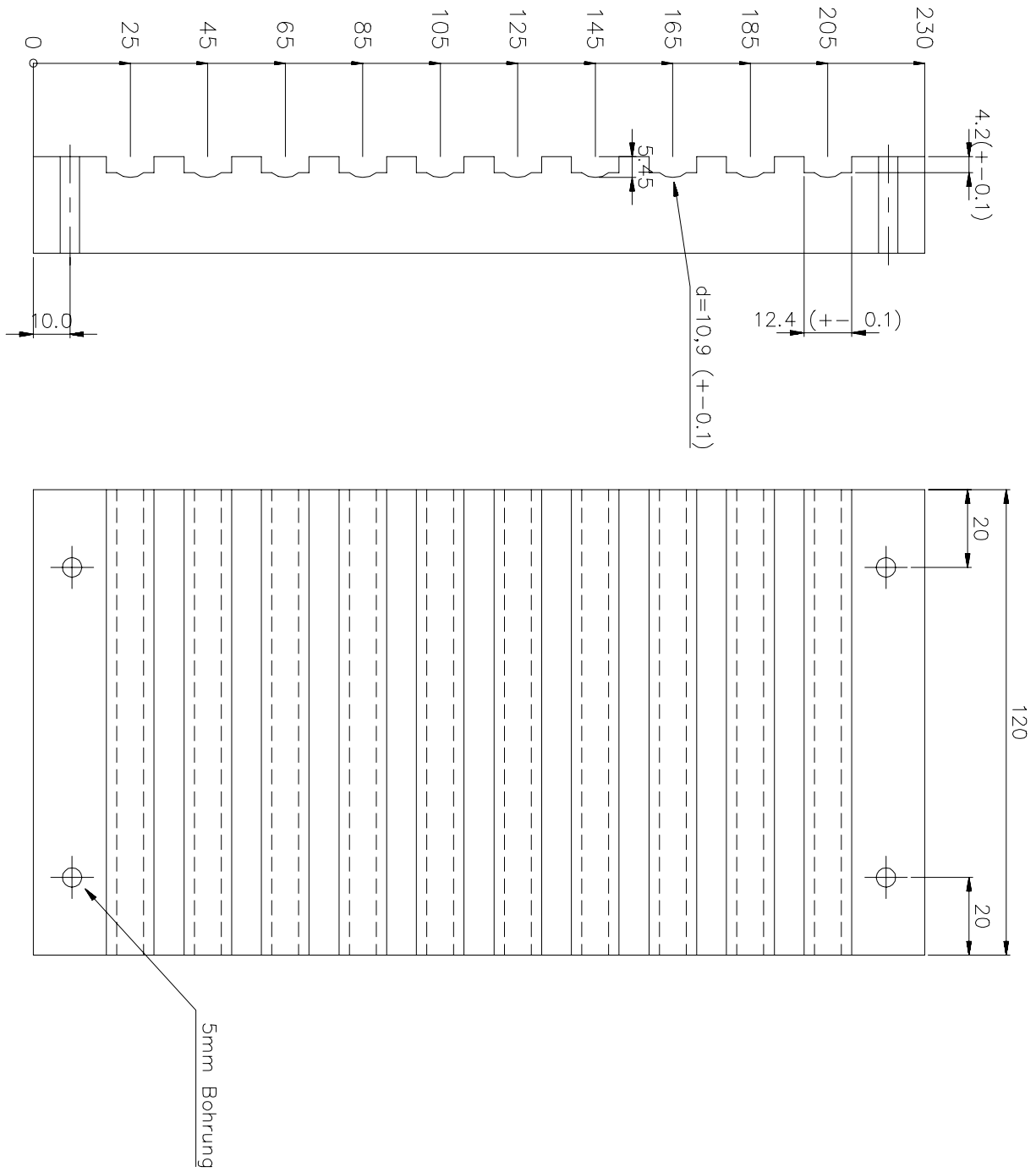


Figure C.16: System to glue hodoscope together

Appendix D

Suppliers

- **Laser diode:** Toshiba TOLD9140
- **Laser diode driver, laser collimator:** Seastar Optics Inc., Sidney, Canada, Fax (604) 655'34'35
- **All mountings, iris, lens:** OWIS GmbH, 7813 Staufen, Germany, Fax (07633) 8'27'27
- **Photo-elastic modulator:** Hinds Instruments Inc., Hillsboro OR, USA, Fax (503) 640'86'95
- **Diffuser:** Oriel Corporation, Stratford CT, USA, Fax (203) 378'24'57
- **Photodiode:** EG & G Optoelectronics, modell number C30808, PARC 5210, Princeton NJ, USA, Fax (609) 883'72'59
- **Preamplifier, Laser Pulser, Temperature Control:** Electronics workshop, Institute of Physics, Basel, CH, plan number SP745, SP 752
- **Lock-in amplifier:** EG & G, PARC 5210, Princeton NJ, USA, Fax (609) 883'72'59
- **Vacuum parts:** CABURN-MDC the Glynde Street East Sussex BN8 6SJ UK, Fax 1273 85'85'61
- **Collimator actuators:** Industrial Device Corporation distributed by: Jo Kell Inc 1011 West 25th Street P.O.Box 11188, Norfolk VA, USA, Fax (804) 627'8773 phone (804)625'5214
- **Target ladder, Lead collimators, Detector stands, Hodoscope mountings:** Mechanics workshop, Institute of Physics, Basel, CH
- **Hodoscope PM's:** Hamamatsu Richtersmattweg Schüpfen CH, FAX 031 879'18'74, phone 031 879'13'33

-
- **Pb-glass PM's:** Philips XP 4512B, Philips Components, Allmendstr. 140, 8027 Zürich, CH, FAX 01 481'77'30, phone 01 488'22'11
 - **Hodoscope scintillators:** Bicron, P.O.B. 3093, 3760 DB Soest, the Netherlands, Fax 31 2155'29214, phone 31 2155'29700
 - **Pb-glass:** Schott Glaswerke, Optisches Glas, Hattenbergstrasse 10, W-6500 Mainz, Germany, FAX 0 6131 66'20'33, phone 0 6131 66'24'21
 - **Large Vacuum cans:** Meyer Tool, USA bought by CEBAF
 - **superconducting splitcoil:** OXFORD
 - **Target foils:** Goodfellow, Cambridge Science Park, Cambridge, CB4 4DJ, England, FAX +44 (0)1223 420'639, phone +44 (0)1223 568'068
 - **Laser splitter cable:** Matrix Elektronik AG, Kirchweg 24, 5422 Oberehrendingen, Switzerland, FAX 056 220'757, phone 056 220'563
 - **Fiber bundle coupler :** Albert D. King, Laser Technology, 4365 E. Pierceville/Monroe St., Milan IN 47031 USA, Fax 001 812 654'3520, phone 001 812 654'2355
 - **Thermal optical glue CARGILLE MELT MOUNT Cat. 24150, Code 5870 nD = 1.582, nC = 1.577, nF = 1.595:** R.P. Cargille Labs. Cedar Grove, N.J. 07009-1289, phone 001 201 239'6633
 - **Peltier elements:** IC Interconnex AG, Hardstrasse 10, 5600 Lenzburg, Sitzerland, Fax 064 52'07'84, phone 064 52'00'84
 - **Pt 100 thermosensor:** Walter Elektronik AG, Frauenfelderstrasse 49, 8370 Sirnach, Switzerland, Fax 0073 26'37'17, phone 073 26'40'40
 - **Target ladder bushings:** Credimex AG, Postfach 6060 Sarnen, Switzerland, Fax 041 66'18'17, phone 041 66'85'30
 - **Densimet parts:** Metallwerk Plansee GmbH, Siebenbürgenstrasse 23, D-86983 Lechbruck, Fax 088 62 773'0, phone 088 62 773'44

Bibliography

- [Bl30] F. Bloch, *Z. f. Phys.* 61, 206, 1930
- [Hu32] H. R. Hulme. *Proc. Royal Soc., A* 135 (1932)
- [Mo32] C. Møller *Ann. Phys.* 14 (1932) 531
- [La60] L.D. Landau and E.M. Lifshitz. *Electrodynamics of continuous media*. Addison-Wesley, Reading MA, 1960
- [Pe60] P.S. Pershan. Magneto-optical effects. *J. Appl. Phys.*, 38 (60) 1482
- [Sc67] D.M. Schwartz, *Phys Rev* 162 (67) 1306
- [Da68] H. Danan, A. Herr and A.J.P. Meyer, *J Appl Phys* 39 2 (68) 669
- [Re69] R.A. Reck and D.L. Fry, *Phys Rev* 184 (69) 492
- [Coo75] P.S. Cooper, *PhD Thesis*, Yale University, 1975 and *A polarized electron target for Møller scattering*, Yale University, 1974
- [Co75] Cooper et al. *Phys. Rev. Lett.* 34 (1975) 1589
- [Al76] Alguard et al. *Phys. Rev. Lett.* 17 (1976) 1261
- [Pr78] Prescott et al. *Phys. Rev. Lett. B* 77 (1978) 347
- [Ray80] Program Raytrace, *University of Virginia*, 1980
- [RT81] Program Radtail, *Richard York, University of Virginia*
- [Gr82] C.D. Graham Jr., *J Appl Phys* 53 (82) 2032
- [Pa82] R. Pauthenet, *J Appl Phys* 53 (82) 2029, 8187
- [Ba83] Baum et al. *Phys. Rev. Lett.* 51 (1983) 1135
- [Br85] Brefeld et al. *Nucl. Instr. and Meth.* 228 (1985) 228
- [Fl86] G.D. Fletcher, T.J. Gay and M.S. Lubell *Phys Rev A* 34 (86) 911
- [LB86] Landolt-Börnstein, *New Series III/19a* (86)

-
- [Do86] T.W. Donnely, A.S. Raskin *Ann. Phys.* 169 (1986) 247
- [Ge86] Gertsen, Kneser, Vogel, *Physik* page 217, 282
- [PP86] Particle properties data booklet, (86) 77
- [Wa86] B. Wagner, *PhD Thesis*, Mainz University, 1986; Equation [3.3] must be multiplied with m .
- [Ja87] J.P. Jakubovics, *Magnetism and magnetic materials* (87)
- [PP90] Particle properties data booklet, American Institute of physics, Berkeley and CERN
- [Wa90] Wagner et al. *Nucl. Instr. and Meth. A* 294 (1990) 541
- [Cr91] John Crangle, *Solid State Magnetism* (91) 168
- [Sc91] M.R. Scheinfein, *Phys Rev B* 43 4 (91) 3395
- [Ze91] W. Bas Zeper, Magneto-optical recording media, PhD theses from Philips Research Laboratory NL, 1991
- [Ar92] J. Arington et al., *Nucl. Instr. and Meth. A* 311 (1992) 39-48
- [PP92] Particle properties data booklet, (92) 114
- [An93] Anthony et al. *Phys. Rev. Lett.* 71 (1993) 959
- [Le94] L.G. Levchuk, *Nucl. Instr. and Meth. A* 345 (1994) 496
- [Ro94] S. Robinson, *PhD Thesis*, University of Basel, 1994.
- [Be95] Beard et al. *Nucl. Instr. and Meth. A* 361 (1995) 46
- [Fe95] A. Feltham and Ph. Steiner, in Proceedings of the Conference on Perspectives in Nuclear Physics at Intermediate Energies, Trieste, Italy, May 1995
- [Sw95] M. Swartz, *Nucl. Instr. and Meth. A* 363 (1995) 526
- [Fe96] A. Feltham and Ph. Steiner, in International Workshop on Polarized Beams and Targets Colonge, Germany June 6-9 (1995) 333
- [Fe97] Feltham et al. *Nucl. Instr. and Meth. A coincidence Møller polarimetry at SLAC, to be published*

Curriculum Vitae

Am 6. September 1966 wurde ich, Matthias Loppacher, geboren als Sohn von Elisabeth und Walter Loppacher. Von 1973 bis 1978 besuchte ich die Primarschule und von 1978 bis 1981 die Sekundarschule in Reinach BL. 1981 trat ich in das Gymnasium Münchenstein BL über, welches ich im Herbst 1985 mit der Matura Typus C beendete. Im Oktober 1986 begann ich an der Universität Basel das Studium der Experimentalphysik mit den Nebenfächern Mathematik und Astronomie. Im Oktober 1991 folgte der Studienabschluss mit dem Diplom.

Seither arbeitete ich unter der Leitung von Prof. Dr. I. Sick am Aufbau von dem Møllerpolarimeter für das Kernphysiklabor CEBAF in Virginia, USA. Die internationalität des Projektes verlangte diverse USA-Aufenthalte – total verbrachte ich während 12 Aufenthalten etwa 9 Monate in den Staaten. Zudem arbeitete ich an verschiedenen Hadronstreuexperimenten unserer Gruppe am Injektorzyklotron des Paul-Scherrer-Institutes mit. Neben meiner Forschertätigkeit war ich als Assistent mit der Betreuung der Studenten während der Projektstudie 4MV beauftragt. Im weiteren Verlaufe übernahm ich die Betreuung der Studenten während des Anfängerpraktikums.

Meine Ausbildung in den Fächern Experimentalphysik, Theoretische Physik, Mathematik und Astronomie verdanke ich folgenden Dozentinnen und Dozenten:

K. Alder, G. Backenstoss, C. Bandle, E. Baumgartner, N. A'Campo, J. Fünfschilling, H. -J. Güntherodt, H. Kraft, P. Oelhafen, G. R. Plattner, H. Rudin, B. Scarpellini, I. Sick, U. Steinlin, G. Tamman, L. Tauscher, H. Thomas, D. Trautmann, C. Trefzger, R. Wagner, I. Zschokke.